

Multi-modal Evidential Fusion Network for Trusted PET/CT Tumor Segmentation

Yuxuan Qi^{a,1}, Li Lin^{b,c,1}, Jingya Zhang^d, Jiajun Wang^{a,*}, Bin Zhang^e

^aSchool of Electronic Information, Soochow University, Suzhou, 215031, China

^bDepartment of Electrical and Electronic Engineering, the University of Hong Kong, Hong Kong, 999077, China

^cDepartment of Electronic and Electrical Engineering, Southern University of Science and Technology, Shenzhen, 518055, China

^dSchool of Electronic and Information Engineering, Changshu Institute of Technology, Suzhou, 215506, China

^eDepartment of Nuclear Medicine, the First Affiliated Hospital of Soochow University, Suzhou 215006, Peoples Republic of China

Abstract

Accurate segmentation of tumors in PET/CT images is important in computer-aided diagnosis and treatment of cancer. The key issue of such a segmentation problem lies in the effective integration of complementary information from PET and CT images. However, the quality of PET and CT images varies widely in clinical settings, which leads to uncertainty in the modality information extracted by networks. To take the uncertainty into account in multi-modal information fusion, this paper proposes a novel Multi-modal Evidential Fusion Network (MEFN) comprising a Cross-Modal Feature Learning (CFL) module and a Multi-modal Trusted Fusion (MTF) module. The CFL module reduces the domain gap upon modality conversion and highlights common tumor features, thereby alleviating the needs of the segmentation module to handle modality specificity. The MTF module utilizes mutual attention mechanisms and an uncertainty calibrator to fuse modality features based on modality uncertainty and then fuse the segmentation results under the guidance of Dempster-Shafer Theory. Besides, a new uncertainty perceptual loss is introduced to force the model focusing on uncertain features and hence improve its ability to extract trusted modality information. Extensive comparative experiments are conducted on two publicly available PET/CT datasets to evaluate the performance of our proposed method whose results demonstrate that our MEFN significantly outperforms state-of-the-art methods with improvements of 2.15% and 3.23% in DSC scores on the AutoPET dataset and the Hecktor dataset, respectively. More importantly, our model can provide radiologists with credible uncertainty of the segmentation results for their decision in accepting or rejecting the automatic segmentation results, which is particularly important for clinical applications. Our code will be available at <https://github.com/QPaws/MEFN>.

Keywords: Tumor segmentation, PET/CT, Multimodal fusion Network, Dempster-Shafer theory, GAN

1. Introduction

PET (Positron Emission Tomography) and CT (Computed Tomography) serve as two major medical imaging techniques that play crucial roles in cancer diagnosis and treatment. CT images provide high-resolution anatomical information for tumor localization and edge detection and hence many researchers in recent years (Li et al., 2018; Yu et al., 2019) developed algorithms for the segmentation of tumor regions in the liver from CT images. However, they may struggle to precisely identify tumor boundaries due to density differences. PET images, on the other hand, measure the level of metabolic activity which reflects the functional status of tissues and cells and offers advantages for disease diagnosis and monitoring. Nevertheless, their lower resolution can lead to relatively blurred tumor boundaries and anatomical structures, which makes it difficult to meet the demands for segmentation accuracy. The complementarity of the CT and PET pushes the simultaneous examination with these two imaging modalities, which urges the development of

joint tumor segmentation algorithms from PET/CT multi-modal images (Islam et al., 2023).

In radiology, tumor segmentation plays a critical role in accurate diagnosis and treatment. The most critical challenge in multimodal segmentation is how to fuse the information from multiple modalities. Existing multimodal fusion methods can be categorized into three types: input-level fusion, feature-level fusion, and decision-level fusion. In input-level fusion, PET and CT images are typically fused by concatenation (Zhang et al., 2015; Chen et al., 2018). However, PET/CT joint segmentation requires capturing complementary information between the two modalities but this fusion approach often struggles to explore nonlinear relationships between modalities, making it difficult to fully utilize the inter-modality information. In feature-level fusion, high-dimensional features from different modalities are typically extracted separately and then combined together. However, simple feature fusion (Zhao et al., 2018) will introduce redundant or conflicting features, which can degrade network performance. Additionally, unlike MR/CT, there are significant feature differences between PET and CT modalities, which further complicates feature fusion process. In decision-level fusion, researchers often use different segmentation networks to segment tumors in individual modalities separately (Nie et al., 2016). The segmentation results of each modality

*Corresponding author.

Email addresses: 20225228030@stu.suda.edu.cn (Yuxuan Qi), linli@eee.hku.hk (Li Lin), zhangjy0611@163.com (Jingya Zhang), jjwang@suda.edu.cn (Jiajun Wang), zbnuc1md@126.com (Bin Zhang)

¹Yuxuan Qi and Li Lin contributed equally to this study.

are then fused using specific fusion strategies (Rokach, 2010) to obtain the final segmentation result. However, in practical clinical applications, the quality of multi-modal data is often unstable (e.g., some modalities may be corrupted), so the quality of multi-modal inputs should be quantitatively measured in some way to provide doctors with predicting confidence, which is particularly important when deploying multi-modal segmentation models for clinical tasks (Ma et al., 2023).

With the development of deep learning, more and more deep neural networks (especially the convolutional neural networks (CNNs)) have been developed for segmenting tumors from medical images of different modalities. For deep segmentation models, the initialization of weights in neural networks significantly impacts their optimization. For instance, random initialization often leads to gradient vanishing, gradient explosion, or entrapment in saddle points and local optima during the optimization process, which renders the network difficult to train. To address these issues, authors in (Glorot and Bengio, 2010) took into account the variances of inputs and outputs and proposed the Xavier initialization method. This method maintains the gradient magnitudes of all layers approximately equal, which can help mitigate the problems of gradient vanishing or explosion and makes it suitable for training deep neural networks. However, for certain specific neural network architectures or activation functions (such as ReLU), gradient vanishing still persists. The authors in (He et al., 2015) devised the Kaiming initialization specifically for the ReLU activation function, which not only effectively avoids the issue of gradient vanishing and enhances the training efficiency but also improves performance of the network. Nonetheless, it is still not applicable to all activation functions. The orthogonal initialization method is another weights initialization strategy proposed in (Saxe et al., 2013) where weights were initialized by generating orthogonal matrices. This strategy can prevent mutual influence between weight matrices, thus aiding in reducing overfitting and improving the network’s generalization ability. However, this algorithm has a higher complexity and is not suitable for all neural network structures. Additionally, the aforementioned initialization methods are based on generic neural networks rather than a specific task. Therefore, in scenarios with high task difficulty (such as PET/CT segmentation), these methods still exhibit sub-optimal performance.

This paper aims to address the aforementioned issues and proposes a Multi-modal Evidential Fusion Network (MEFN) to achieve more accurate and reliable PET/CT multi-modal tumor segmentation. Specifically, this network comprises two main modules: the Cross-Modal Feature Learning (CFL) module for modality transfer and the Multi-modal Trusted Fusion (MTF) module for tumor segmentation. In CFL, we use GAN to enable back-and-forth transformation between the two modalities and set additional decoupling branches for the network to extract tumor features. The intuition behind this is that during the modality transformation process, the network can simultaneously learn the content features of both modalities. The proposed Multi-scale Tumor Guided Attention (MTGA) can assist the network in focusing more on extracting features from the tumor area and hence provides useful tumor information for

subsequent segmentation. Then, the trained network parameters in CFL are transferred to the segmentation backbone of MTF and shared as the initial weights of the network during training. Such a task-driven weights initialization strategy can effectively improve the convergence speed, alleviate the aforementioned training challenges and achieve better performance. In MTF, in addition to the segmentation backbone, we also introduce the Dual-attention Feature Calibrating (DFC) module and adopt the Dempster-Shafer Theory Based Trusted Fusion (DBTF) method. These two methods respectively address feature-level fusion and decision-level fusion. Unlike previous fusion methods, our feature-level fusion takes into account the importance of weight allocated for different modalities and calibrates the semantic features extracted from each modality based on their confidence to minimize the impact of redundant and conflicting features on the network. The DBTF method, based on the Dempster-Shafer theory, performs decision-level fusion by considering the quality differences between different modalities and making fusion decisions based on uncertainty, thus fusing the segmentation results of different modalities both accurately and reliably.

In summary, this work makes the following three main contributions:

- A novel task-driven initialization method named CFL is proposed to alleviate the impact of improper weights initialization on network optimization.
- A feature-level fusion method named DFC is introduced to provide a more reasonable weight allocation for feature fusion by reducing the impact of redundant and conflicting features.
- To handle the quality differences between the modalities, a decision-level fusion strategies is proposed to allocate fusion weights based on the uncertainty between different modalities in an interpretable manner.
- Extensive experiments on two large PET/CT public datasets demonstrate that the proposed method outperforms state-of-the-art multi-modal segmentation algorithms. Ablative experiments are conducted to demonstrate the effectiveness and robustness of the individual modules proposed in our work from different perspectives.

2. Related work

2.1. Generative adversarial model

Generative Adversarial Networks (GANs) are based on zero-sum games in game theory and consist of a generator and a discriminator (Goodfellow et al., 2020). The generator creates data by learning its original distribution while the discriminator differentiates between real and generated data and hence guides the generator toward more realistic outputs. GAN is often used for data reconstruction (Wolterink et al., 2017; Wang et al., 2018), synthetic data generation (Bowles et al., 2018) and converting data between modalities (Ben-Cohen et al., 2019). For

example, upon incorporating tumor segmentation labels into the generator, authors in (Bi et al., 2017) attempted to synthesize PET from CT using a conditional GAN (cGAN). However, this method is impractical for us as segmentation labels are the target predictions in our task. In (Zhang et al., 2022), the authors proposed Modality-Specific Segmentation Networks with integrated cGAN to extract common features from PET and CT images for lung tumor segmentation. However, this method merges image synthesis with segmentation tasks, which makes the computational overhead high. In (Zhang et al., 2021), a Cross-modal Feature Transition module was introduced with cycleGAN to facilitate cross-modal knowledge transfer, which aims to improve segmentation by using multi-modal information. This method, however, doesn't focus enough on the modal differences crucial for segmentation in tumor areas. Motivated by the aforementioned method, we propose the Cross-Modal Feature Learning (CFL) module where the Multi-scale Tumor Guided Attention (MTGA) mechanism is introduced to assist concentrating on tumor areas while learning cross-modal features and reducing modal differences, thus enabling the network to learn the task-driven initial weights that are helpful for multi-modal tumor segmentation.

2.2. Uncertainty estimation

In clinical practice, AI often lacks sufficient decision-making information, which makes it crucial to quantify uncertainty for safe application (Begoli et al., 2019). Current research on uncertainty estimation includes Bayesian (Gal and Ghahramani, 2016), ensemble (Lakshminarayanan et al., 2017), deterministic (Van Amersfoort et al., 2020) and evidence-based methods (Huang et al., 2022). Bayesian methods in neural networks replace fixed parameters with probability distributions, leading to probabilistic output labels. For example, Monte Carlo dropout (MC dropout) is introduced as a Bayesian approximation in (Gal and Ghahramani, 2016), where dropout layers are used in multiple inference runs to mimic a Gaussian process. Although this strategy is computationally less demanding, it leads to inconsistent outputs (Kohl et al., 2018). Ensemble methods improve neural network classification by using model averaging for uncertainty estimation, involving training multiple models with random initialization and adversarial training (Kamnitsas et al., 2018; Lakshminarayanan et al., 2017). While this method doesn't require altering the network architecture, it necessitates retraining models from scratch and hence incurs high computational costs for complex models. Deterministic-based methods, like Deep deterministic uncertainty (Mukhoti et al., 2021), have been extended to semantic segmentation using feature space density. However, they alter network structure and increase computational costs. A recent study (Huang et al., 2022) suggested using deep feature extraction and evidence layers for segmenting lymphoma in PET and CT scans. Rather than to obtain more robust segmentation by calibrating the uncertainty, these studies tried to improve the performance of segmentation upon guiding the uncertainty. They only utilized the generated uncertainty to evaluate the segmentation results but not to further optimize the network training. Instead, our ap-

proach introduces not only an Uncertainty Perceptual Loss for robust segmentation by forcing the network focusing on the prediction results of regions with large uncertainty during training but also an Uncertainty Calibrator (UC) to further refine network training by calibrating the extracted semantic information according to uncertainty.

2.3. Multi-modal fusion

Multi-modal medical image segmentation, essential for accurately identifying tumors, employs various fusion strategies: input-level, feature-level and decision-level fusion. A typical example of input-level fusion is the 3D-Inception ResNet proposed in (Qayyum et al., 2021) which combined PET and CT images in channel-wise manner. Some recent studies (Wang et al., 2021; Liu et al., 2021) employed attention mechanisms in their models to allocate varying weights to different modality spaces and achieved fairly better results. Although the input-level fusion preserves the original details of the image, it fails in utilizing of the interrelations between different modalities. Feature-level fusion trains networks with individual modal images and then fuses features of different modalities across layers for final segmentation. It can effectively integrate and utilize multi-modal images (Zhou et al., 2019). Most existing methods in literature fuse multi-modal features by directly combining features of each modality (Zhong et al., 2018), which potentially miss key information and introduce redundancies and hence hinder network performance. Ahmad et al. (2023) introduced the Anatomy Aware Tumor Segmentation Network (AATSN), which uses an encoder to extract CT anatomical and an encoder to extract PET metabolic features for a lightweight fusion attention decoder. In this way, the decoder can use CT for spatial and PET for metabolic reference and hence improves tumor segmentation. However, its lightweight attention mechanism might under-perform with complex data due to limited training parameters. Decision-level fusion employs separate networks for each modality image. Each network uses its modality specific information whose outputs are integrated for the final result. Conventional fusion strategies include averaging and majority voting (Rokach, 2010). Kamnitsas et al. (2018) used an averaging strategy where the authors trained three networks and averaged their confidence scores for voxel segmentation. The majority voting strategy assigns voxels the most frequent label from all networks. However, these methods often overlook the uncertainty in each modality and lead to potential errors in probabilistic fusion, which is fatal in clinical practice. Huang et al. (2021a) combined PET and CT results using a Dempster-Shafer Theory-based fusion layer in 3D UNet. But this method, limited to decision layer fusion, shows less efficiency in handling multi-modal information. To resolve this problem, this paper merges feature-level and decision-level fusion strategies with the Dual-attention Feature Calibrating (DFC) module and Dempster-Shafer Theory Based Trusted Fusion (DBTF) method, respectively. DFC reduces feature redundancies and calibrates low-confidence outputs. It's worth noting that, differing from Huang et al. (2021a), our DBTF fuses PET and CT data based on uncertainty and mutual information, which greatly improves multi-modal fusion efficiency.

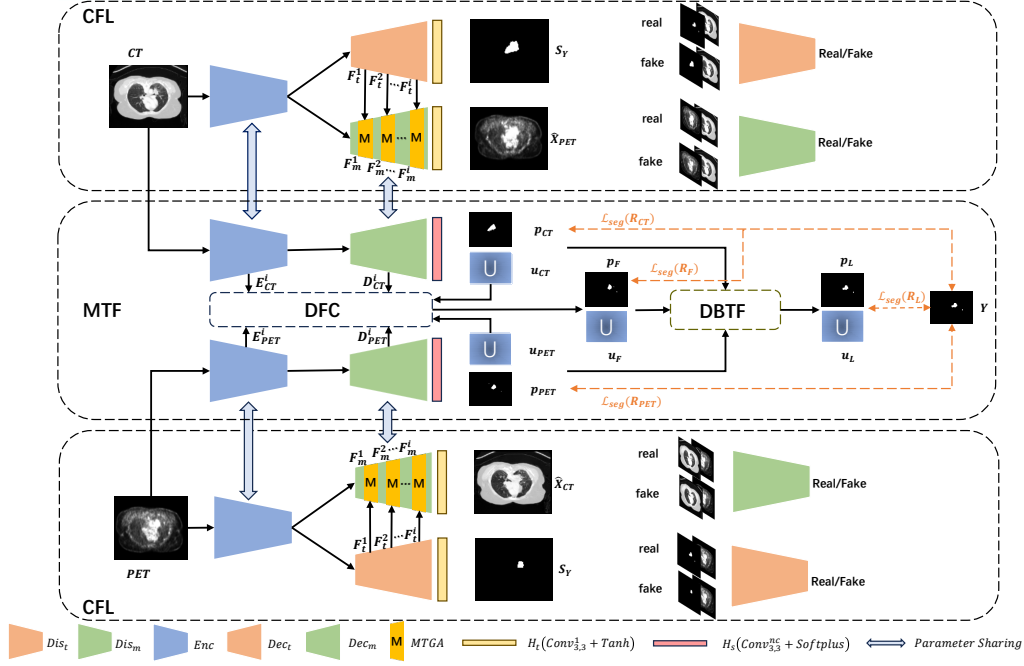


Fig. 1. Framework of our proposed MEFN which consists of CFL module and MTF module, both with two branches for PET and CT, respectively. For simplicity, Enc represents the encoder Enc^{CT} or Enc^{PET} , Dec_m represents the modality decoder Dec_m^{CT} or Dec_m^{PET} , Dec_t represents the tumor decoder Dec_t^{CT} or Dec_t^{PET} , Dis_m represents the modality discriminator Dis_m^{CT} or Dis_m^{PET} , Dis_t represents the shared tumor discriminator.

3. Methodology

In this section, we commence by succinctly outlining the MEFN framework, before delving into a comprehensive exposition of its three pivotal components: the Cross-Modal Feature Learning (CFL) module, the Dual-attention Feature Calibrating (DFC) module and the Dempster-Shafer Theory Based Trusted Fusion (DBTF). The overall framework of MEFN is provided in Fig. 1.

3.1. Overview of MEFN

Defining CT image as X_{CT} and PET image as X_{PET} , the two inputs (X_{CT} and X_{PET}) are first fed into the CFL. Within the CFL, it orchestrates the generation of pseudo PET images \hat{X}_{PET} and pseudo CT images \hat{X}_{CT} for each modality through adversarial training. Concurrently, an auxiliary tumor decoder branch Dec_t produces corresponding artificial tumor mask images S_Y . In the training phase, the network acquires modality-specific features of CT and PET along with general tumor features, thereby minimizing the disparities between modalities. Subsequently, the network parameters trained in the CFL are transferred to the segmentation backbone as the initial weights of the network, therefore accelerating the convergence speed and reducing the risk of falling into local minima under the task-driven initialization of weights. Next, the encoder and decoder features from the two segmentation backbones are fed into the DFC. Within the DFC, encoder and decoder features undergo two distinct fusion strategies: in terms of Cross Modality Attention (CMA) and in terms of Uncertainty Calibrator (UC), respectively. The former adaptively adjusts features extracted by

the encoder through mutual attention, which significantly reduces feature redundancies and enhances fusion efficiency. The latter calibrates semantic features extracted by the network using uncertainty factors, which forces the network focusing on areas of high uncertainty within modalities and thus diminishes feature confliction between modalities and enhancing fusion accuracy. Features refined by CMA and UC are then input into the fusion decoder Dec_f to obtain the fused segmentation results Y_F and U_F after upsampling. Finally, segmentation results from the CT branch (Y_C and U_C), PET branch (Y_P and U_P), along with the merged segmentation results (Y_F and U_F), are collectively processed in terms of DBTF for decision-level fusion. In DBTF, the segmentation results of each branch will dynamically adjust the fusion weight according to the uncertainty, making the fusion result more robust, then the final segmentation outcomes can be acquired as \hat{Y} and U_L . Although the network structures in CFL and MTF are not necessarily the same, the more network layers these two networks share, the richer the modality-specific features can be transferred from CFL to MTF. To this end, we have designed two modules with quite similar network structures and the only difference is the number of kernels set to the decoder's output head. As shown in Fig. 1, the decoder's output head in CFL (H_i) uses one convolutional kernels and employs a $Tanh$ activation function, while the number of convolutional kernels in the decoder's output head in MTF (H_s) corresponds to the number of segmentation classes and a $Softplus$ activation function is utilized in this case. As can be seen, such an MTF network architecture could share the most network layers with the CFL and thus can take full advantage of the features learned from the CFL. The algorithm for the overall

Algorithm 1: The training process of MEFN.

Input: Samples of training set $D = \{x_1^{(n)}, x_2^{(n)}\}_{n=1}^N$, labels of training set $Y = \{y^{(n)}\}_{n=1}^N$, the architecture of MEFN, number of training iterations T , number of minibatch B .

Output: Trained model parameters ϕ .

for $t \leftarrow 1$ to T **do**

$\{x_1^{(b)}, x_2^{(b)}\}, 1 \leq b \leq B \leftarrow D$;

$\{y^{(b)}\}, 1 \leq b \leq B \leftarrow Y$;

// Stage1. Train the CFL.

for $b \leftarrow 1$ to B **do**

Input $x_1^{(b)}, x_2^{(b)}, y^{(b)}$, use *Adam* to update the parameter ϕ in Generator $\{G(x, y; \phi)\}$ and Discriminator $\{D(x, y; \phi)\}$ according to Eq. (5);

end

Output the trained parameters ϕ in Generator.

// Stage2. Train the MTF.

for $b \leftarrow 1$ to B **do**

Initialization segmentation backbone:

$S(x; \phi) \leftarrow \phi$, where ϕ are from $G(x, y; \phi)$ trained in Stage1;

$R_1 = \{\alpha_1^{(b)}, p_1^{(b)}, u_1^{(b)}\} \leftarrow S_1(x_1^{(b)}; \phi)$;

$R_2 = \{\alpha_2^{(b)}, p_2^{(b)}, u_2^{(b)}\} \leftarrow S_2(x_2^{(b)}; \phi)$;

$R_F = \{\alpha_F^{(b)}, p_F^{(b)}, u_F^{(b)}\} \leftarrow DFC(R_1, R_2; \phi)$;

Obtain $R_L = \{\alpha_L^{(b)}, p_L^{(b)}, u_L^{(b)}\}$ according to Eq. (19);

Train the $S_1(\phi)$, $S_2(\phi)$ and $DFC(\phi)$ according to Eq. (14)

end

end

Output trained model parameters ϕ of MEFN.

process of MEFN can be described as in Algorithm 1.

3.2. Cross-modality Feature Learning (CFL)

As illustrated in the top and bottom parts of Fig. 1, our proposed MEFN encompasses two CFL branches with a structure mirrors each other. Taking the CT branch as an example, given the input X_{CT} , the modality encoder Enc^{CT} extracts high-level feature representations of the CT image. Subsequently, the modality decoder Dec_m^{CT} transforms these high-dimensional features into modality-specific features and generates a synthetic PET image \hat{X}_{PET} . Concurrently, the tumor decoder Dec_t^{CT} decouples tumor features from the high-dimensional features of the CT image to produce a synthetic tumor mask image S_Y . Notably, different to the segmentation task, S_Y here represents the generated pseudo tumor mask image, rather than the probability prediction map of the tumor region. The task of modality discriminator Dis_m^{PET} is to distinguish between X_{PET} and \hat{X}_{PET} .

To extract general tumor features across different modalities, a shared tumor discriminator Dis_t is designed to differentiate between real tumor mask Y and synthetic tumor mask S_Y . The architecture of all encoders, decoders and discriminator networks adheres to the framework established by Isola et al. (2017). To further make the network focusing more on tumor features, we introduce the Multi-scale Tumor Guided attention (MTGA) module. MTGA is incorporated at every upsampling stage of Dec_m , where tumor features F_t^i decoupled by Dec_t are sent to Global Average Pooling (GAP) and a Multi-Layer Perceptron (MLP) in MTGA module of Dec_m (See Fig. 2(a)) to learn channel attention. This channel attention is then employed to weight the modality features F_m^i extracted by Dec_m upon element-wise multiplication (\otimes). The detailed description of process flow of MTGA is depicted in Fig. 2(a). Let X represent the input, the operations of Cross-modality Feature Learning module can be mathematically formulated as follows:

$$\begin{cases} (F_t^1, F_t^2, \dots, F_t^n) = Dec_t(Enc(X)) \\ Attn = \sigma(MLP(GAP(Dec_t(Enc(X)))))) \\ (\tilde{F}_m^1, \tilde{F}_m^2, \dots, \tilde{F}_m^n) = Attn \otimes Dec_m(Enc(X)) \\ (F_m^1, F_m^2, \dots, F_m^n) = TransConv(\tilde{F}_m^1, \tilde{F}_m^2, \dots, \tilde{F}_m^n) \\ \hat{X} = H_t(F_m^n) \\ S_Y = H_t(F_t^n) \end{cases} \quad (1)$$

where F_t^i , F_m^i and σ represent the output of the i -th layer of Dec_t , the output of the i -th layer of Dec_m and the sigmoid function, respectively. $TransConv$ represents transposed convolution, \hat{X} represents the generated fake image and S_Y represents the generated tumor mask image. The entire CFL adopts adversarial training under the constraint of two adversarial losses for generating fake PET (or CT) images and for generating fake tumor mask images, respectively. Taking the CT branch as an example, the above mentioned two losses denoted as $\mathcal{L}_{adv_m}^{CT}$ and $\mathcal{L}_{adv_t}^{CT}$ are defined as:

$$\begin{aligned} \mathcal{L}_{adv_m}^{CT}(Gen_m^{CT}, Dis_m^{CT}) = & -E_{X_{CT}, X_{PET}} [\log Dis_m^{CT}(X_{CT}, X_{PET})] \\ & - E_{X_{CT}} [\log(1 - Dis_m^{CT}(X_{CT}, \hat{X}_{PET}))] \end{aligned} \quad (2)$$

$$\begin{aligned} \mathcal{L}_{adv_t}^{CT}(Gen_t^{CT}, Dis_t) = & -E_{X_{CT}, Y} [\log Dis_t(X_{CT}, Y)] \\ & - E_{X_{CT}} [\log(1 - Dis_t(X_{CT}, S_Y))] \end{aligned} \quad (3)$$

where Gen_m^{CT} and Gen_t^{CT} denote $Enc^{CT}-Dec_m^{CT}$ and $Enc^{CT}-Dec_t^{CT}$ encoder-decoder combinations, respectively. Y represents the real tumor mask. Considering the difference between the real target modality and the synthetic target modality, L1 loss is used to ensure that the generated target modality is close to the real target modality, thereby reducing blurriness. The L1 loss $\mathcal{L}_{l_1}^{CT}$ for CT branch can be defined as,

$$\begin{aligned} \mathcal{L}_{l_1}^{CT}(Gen_m) = & E_{X_{PET}, \hat{X}_{PET}} [\|X_{PET} - \hat{X}_{PET}\|_1] \\ & + E_{Y, S_Y} [\|Y - S_Y\|_1] \end{aligned} \quad (4)$$

The same goes for the PET branch, so the loss function \mathcal{L}_{CFL} of the entire CFL can be defined as,

$$\begin{aligned} \mathcal{L}_{CFL} = & \mathcal{L}_{adv_m}^{CT} + \mathcal{L}_{adv_t}^{CT} + \lambda_1 \mathcal{L}_{l_1}^{CT} \\ & + \mathcal{L}_{adv_m}^{PET} + \mathcal{L}_{adv_t}^{PET} + \lambda_1 \mathcal{L}_{l_1}^{PET} \end{aligned} \quad (5)$$

where λ_1 is the hyperparameters used to balance the losses in Eq. (5). In this paper, λ_1 is set as 100.

3.3. Segmentation Backbone and Multimodal Feature-level Fusion

For convenient of parameter sharing, the network architecture of the segmentation backbone is strikingly similar to the Enc_m-Dec_m structure of the CFL, with the only modification being the final output layer. The CFL employs an output head denoted as Ht ($Conv_{3,3}^1+Tahn$), while the segmentation backbone utilizes an output head denoted as Hs ($Conv_{3,3}^{nc}+Softplus$). In pursuit of facilitating multi-modal feature fusion, we propose a novel fusion network. This network introduces a specifically designed fusion branch that leverages single-modality prediction outcomes and the modality's inherent uncertainties (details of which are delineated in section 3.4) to guide the feature fusion process. This approach not only allows for the seamless transfer of features learned from the CFL but also enables the acquisition of potent fusion features, which is instrumental for delineating the tumor regions required for segmentation.

Given modalities CT and PET, the multi-modal feature-level fusion network comprises two mono-modality segmentation branches of $Enc^{CT}-Dec_m^{CT}$ and $Enc^{PET}-Dec_m^{PET}$, as well as a multi-modal feature fusion branch of Dec_f . Herein, the mono-modality segmentation branch $Enc^{CT}-Dec_m^{CT}$ utilizes CT data as input to predict the segmentation mask p_{CT} for the tumor region and its associated uncertainty u_{CT} . Similarly, the mono-modality segmentation branch $Enc^{PET}-Dec_m^{PET}$ employs PET data as input, predicting the segmentation mask p_{PET} for the tumor area and its corresponding uncertainty u_{PET} .

To fuse effectively features from each modality, we introduce a novel Dual-attention Feature Calibrating (DFC) module as depicted in Fig. 2(b) which employs distinct fusion strategies for the encoder and decoder features of the two mono-modality branches. For encoder features, motivated by Vaswani et al. (2017), DFC utilizes Cross Modality Attention (CMA) as illustrated in the lower left part of Fig. 2(b) which first merges features E_{CT}^i and E_{PET}^i from different layers of the two mono-modality branches using query, key and value vectors and then recovers the number of channels of the merged features through a 3×3 convolution to obtain the final fused feature E^i . Here, the query, key and value vectors are all derived from 1×1 convolutions. Upon adaptive adjustments of these vectors, encoder features from each modality are selectively integrated, thereby reducing redundancy and improving fusion efficiency. For decoder features, DFC adopts an Uncertainty Calibrator (UC) as shown in the lower right part of Fig. 2(b). The UC employs the predictive uncertainties u_{CT} and u_{PET} from the two mono-modality segmentation branches as calibrators for the decoder features, thereby refining the extracted semantic information. Specifically, for decoder features D_{CT}^i and D_{PET}^i of different

layers, U_{CT} and U_{PET} are first down-sampled to match the dimensions of D_{CT}^i and D_{PET}^i whose results are then multiplied in element-wise manner by 1×1 convolutional results of D_{CT}^i and D_{PET}^i , respectively. The resultant ones are added residually to D_{CT}^i and D_{PET}^i respectively to alleviate degradation problem. Upon concatenating these two features in channel-wise manner and performing a 3×3 convolution, the fused feature D^i can be derived. In scenarios where the modalities exhibit areas of high uncertainty (typically at boundaries and conflicting features), UC directs the network's focus towards these areas of high uncertainty, thereby improve the network's precision in delineating boundary regions and reducing conflicts between modalities. Ultimately, E^i and D^i are connected in a manner similar to the skip connections in UNet and then fed into the multi-modal fusion branch Dec_f to learn more potent fused features, culminating in the generation of a fused segmentation probability map p_F and fused uncertainty u_F for the tumor region.

Unlike conventional segmentation approaches, our segmentation backbone replaces Softmax in the traditional neural network classifier with Softplus to facilitate the quantification of uncertainty. Thus, the outcomes derived from the segmentation backbone should not be interpreted directly as the predictive segmentation results, but rather as evidence vectors e representing the evidence observed by the model for classification. Consequently, parameters for the Dirichlet distribution can be obtained. For traditional neural network classifiers employing Softmax, the cross-entropy loss is commonly utilized:

$$\mathcal{L}_{ce} = - \sum_{c=1}^C y_X^c \log(p_X^c) \quad (6)$$

where p_X^c and y_X^c are the predicted probability and label that sample X belongs to class c , respectively, C is the number of classification. Due to the aforementioned difference between models with Softmax and those with Softplus, the adjusted cross-entropy loss for our model can be derived by making simple modification with regard to the traditional cross-entropy loss in Eq. (6) and can be formulated as:

$$\begin{aligned} \mathcal{L}_{ace}(\alpha_X) = & \int \left[- \sum_{c=1}^C y_X^c \log(p_X^c) \right] D(p_X | \alpha_X) dp_X \\ = & \sum_{c=1}^C y_X^c (\psi(S_X) - \psi(\alpha_X^c)) \end{aligned} \quad (7)$$

where ψ refers to the digamma function and $D(p_X | \alpha_X)$ is the Dirichlet probability density function over $p_X = [p_X^1, \dots, p_X^C]$ and can be expressed as:

$$D(p_X | \alpha_X) = \begin{cases} \frac{1}{B(\alpha_X)} \prod_{c=1}^C (p_X^c)^{\alpha_X^c-1} & \text{for } p_X \in P_C \\ 0 & \text{otherwise} \end{cases} \quad (8)$$

Herein, $\alpha_X = [\alpha_X^1, \dots, \alpha_X^C]$ (where $\alpha_X^c = e_X^c + 1$ with e being obtained from the segmentation backbone), p_X^c is the projected probability and can be computed as:

$$p_X^c = 1 - \sum_{i \neq c} b_X^i \quad (9)$$

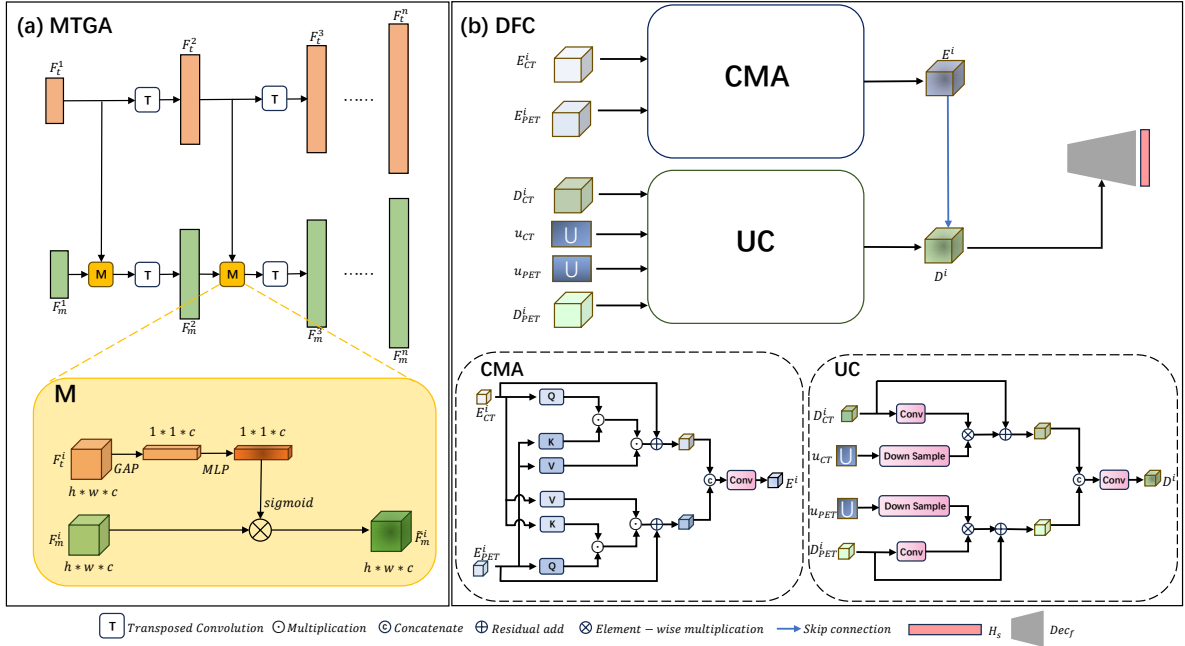


Fig. 2. The architecture of (a) Multi-scale Tumor Guided Attention and (b) Dual-attention Feature Calibrating module.

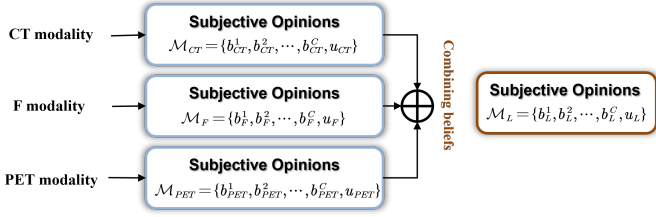


Fig. 3. Schematic illustration of the Dempster-Shafer Theory Based Trusted Fusion.

with $b_X^i = \frac{e_X^i}{S_X} = \frac{\alpha_X^i - 1}{S_X}$ representing the belief mass, where $S_X = \sum_{c=1}^C \alpha_X^c$ representing the Dirichlet strength, $B(\alpha_X) = \int \prod_{c=1}^C (p_X^c)^{\alpha_X^c - 1} dp_X$ denotes the C-dimensional multinomial beta function and P_C is the C-dimensional unit simplex given by:

$$P_C = \{p_X \mid 0 \leq p_X^1, \dots, p_X^C \leq 1\} \quad (10)$$

To ensure that incorrect labels generate less evidence, potentially reducing to zero, a KL divergence loss function is introduced as follows:

$$\mathcal{L}_{KL}(\alpha_X) = \log \left(\frac{\Gamma(\sum_{c=1}^C \tilde{\alpha}_X^c)}{\Gamma(\tilde{\alpha}_X^c)} \right) + \sum_{c=1}^C (\tilde{\alpha}_X^c - 1) \left[\psi(\tilde{\alpha}_X^c) - \psi\left(\sum_{c=1}^C \tilde{\alpha}_X^c\right) \right] \quad (11)$$

where Γ is the gamma function, $\tilde{\alpha}_X^c = y_X^c + (1 - y_X^c) \odot \alpha_X^c$ (\odot means element-wise multiplication) represents the adjustment parameters for the Dirichlet distribution employed to ensure that the evidence for the ground-truth class is not mistakenly considered to be zero. Moreover, due to the fact that the Dice

score is a crucial metric for evaluating the performance of tumor segmentation, we employ the following soft Dice loss to optimize the network:

$$\mathcal{L}_{Dice}(p_X) = \sum_{c=1}^C \left(1 - \frac{2y_X^c p_X^c + smooth}{y_X^c + p_X^c + smooth} \right) \quad (12)$$

where $smooth$ represents the smooth coefficient which is empirically set to 1×10^{-5} in our work. Furthermore, to force the network focusing more on prediction results for areas with greater uncertainty, we introduce the following Uncertainty Perceptual Loss:

$$\mathcal{L}_{UP}(p_X, u_X) = -u_X \sum_{c=1}^C y_X^c \log(p_X^c) \quad (13)$$

where u_X represents the uncertainty mass of the sample X which will be defined in section 3.4.

Given the substantial uncertainty in the model during the initial stages of training, to mitigate the impact of excessive uncertainty on model optimization, an annealing factor $(1 - \beta_t)$ is employed, with $\beta_t = \beta_0 e^{-\frac{\ln \beta_0}{T} t}$ while T and t represent the total number of epochs and the current epoch, respectively. Therefore, for the segmentation result $R_{CT} = \{\alpha_{CT}, p_{CT}, u_{CT}\}$ of CT, the overall segmentation loss function of our proposed network can be defined as follows:

$$\mathcal{L}_{seg}(R_{CT}) = (1 - \beta_t) \mathcal{L}_{acc}(\alpha_{CT}) + \beta_t \mathcal{L}_{UP}(p_{CT}, u_{CT}) + \mathcal{L}_{KL}(\alpha_{CT}) + \mathcal{L}_{Dice}(p_{CT}) \quad (14)$$

Similarly, for the segmentation results $R_{PET} = \{\alpha_{PET}, p_{PET}, u_{PET}\}$ of PET and the fused segmentation result $R_F = \{\alpha_F, p_F, u_F\}$, the segmentation losses $\mathcal{L}_{seg}(R_{PET})$ and $\mathcal{L}_{seg}(R_F)$ are derived in the same manner.

3.4. Uncertainty Quantification and Dempster-Shafer Theory Based Trusted Fusion

Guided by Subjective Logic (Jsang, 2018) and based on the evidence gathered within the data, we may deduce an overall uncertainty (uncertainty masses) as well as probabilities for different categories (belief masses). Here, evidence denotes indicators collected from the input that support categorization, intimately linked to the density parameters of the Dirichlet distribution as discussed in section 3.3. Based on the evidence vector e output from the network, we can ascertain the parameters α_X of the Dirichlet distribution. Specifically, for a C -class problem, the subjective logic endeavors to allocate a belief mass to each category label and an overall uncertainty mass to the framework as a whole. Hence, for any modality X , the C belief mass values $b_X^c (c = 1, 2, \dots, C)$ and the overall uncertainty u_X are non-negative and are cumulatively equating to one:

$$u_X + \sum_{c=1}^C b_X^c = 1 \quad (15)$$

Thus, the overall uncertainty u_X can be articulated as follows:

$$u_X = 1 - \sum_{c=1}^C b_X^c = \frac{C}{S_X} \quad (16)$$

Eq. (16) implies that the more the evidence is observed for category c , the greater the probability will be assigned to c and hence the less the overall uncertainty is. Conversely, the less evidence is observed in total, the greater the overall uncertainty will be. Belief assignments can be regarded as a form of subjective opinion.

Intuitively, the fused prediction of modalities X_1 and X_2 with high uncertainty (large u_{X_1} and u_{X_2}) must possess low confidence (small b^c). Conversely, if the uncertainties of both modalities are low (small u_{X_1} and u_{X_2}), the final prediction may exhibit higher confidence (large b^c). When only one modality demonstrates low uncertainty (only u_{X_1} or u_{X_2} is large), the final prediction relies solely on the modality with lower uncertainty. Hence, we employ the Dempster-Shafer Theory of Evidence (DST) to achieve our objectives. As shown in Fig. 3, DST allows for the combination of evidence from different sources, which culminates in a belief (belief function) that considers all available evidence. Defining $M_{X_i} = \left\{ \left\{ b_{X_i}^c \right\}_{c=1}^C, u_{X_i} \right\}, (i = 1, 2)$ as the set of probability mass allocated for a single modality X_i , then the joint mass $M = \left\{ \left\{ b^c \right\}_{c=1}^C, u \right\}$ for modalities X_1 and X_2 can be defined as follows:

$$M = M_{X_1} \oplus M_{X_2} \quad (17)$$

where \oplus denotes the set operations defined as follows:

$$b^c = \frac{1}{1 - \text{Cof}} \left(b_{X_1}^c b_{X_2}^c + b_{X_1}^c u_{X_2} + b_{X_2}^c u_{X_1} \right) \quad (18)$$

$$u = \frac{1}{1 - \text{Cof}} u_{X_1} u_{X_2}$$

Herein, $\text{Cof} = \left(\sum_{i \neq j} b_{X_i}^i b_{X_j}^j + b_{X_1}^i u_{X_2} + b_{X_2}^j u_{X_1} \right) + u_1 u_2$ represents the extent of confliction between two sets of masses and

$\frac{1}{1 - \text{Cof}}$ is employed for normalization purposes. In this work, to improve the efficiency of fusion, we also incorporate the results of the DFC in addition to CT and PET modalities as a new modality F into the decision-level fusion. Therefore, the final fusion function can be defined as follows:

$$M_L = M_{CT} \oplus M_{PET} \oplus M_F \quad (19)$$

Upon obtaining the joint mass $M_L = \left\{ \left\{ b_L^c \right\}_{c=1}^C, u_L \right\}$, according to Eq. (16), the corresponding joint evidence e_L^c and Dirichlet distribution parameters α_L^c are derived from multiple perspectives as follows:

$$S_L = \frac{C}{u_L}, e_L^c = b_L^c \times S_L, \alpha_L^c = e_L^c + 1 \text{ and } p_L^c = b_L^c + u_L^c \quad (20)$$

Following the aforementioned fusion rules, we can obtain the estimated multi-modal joint evidence $e_L = [e_L^1, \dots, e_L^C]$ and the corresponding parameters of the joint Dirichlet distribution $\alpha_L = [\alpha_L^1, \dots, \alpha_L^C]$ as well as the final prediction of the multi-modal trusted fusion $p_L = [p_L^1, \dots, p_L^C]$ and the overall uncertainty u_L . For deep supervision of network training, the final segmentation result $R_L = \{ \alpha_L, p_L, u_L \}$ from decision-level fusion can be obtained in a similar manner to the previously defined Eq. (14) for the loss $\mathcal{L}_{seg}(R_L)$.

4. Experiments and discussions

4.1. Datasets and preprocessing

The proposed segmentation framework is evaluated on two public PET/CT datasets, with one originating from the 25th MICCAI Challenge on publicly available whole-body PET/CT dataset (AutoPET) (Gatidis et al., 2022) and the other from the 23rd MICCAI Challenge on head and neck tumors segmentation in PET/CT (Hecktor) (Oreiller et al., 2022).

The AutoPET dataset comprises 900 histologically confirmed malignant melanoma, lymphoma or lung cancer patients from two large medical centers in Germany who undergo PET/CT examinations. Two experienced radiologists manually delineate all tumor regions, tasked with whole-body tumor segmentation.

The Hecktor dataset consists of 882 patients with primary tumors and with gross tumor volumes of the head and neck from four different centers. All patients undergo FDG-PET/CT imaging scans within 18 days before treatment (range: 6-66). It contains two segmentation tasks, one for the primary tumor (GTVp) in the head and neck and another for the involved lymph nodes (GTVn).

Given data from multi-centers, we normalize the CT and PET images. The CT volumes are clipped to [-1024, 1024] Hounsfield units and then mapped to [-1, 1]. We normalize the PET using the Z-score. As the segmentation is performed in 2D, we sliced the 3D datasets. Similar to the work proposed by Fu et al. (Fu et al., 2021), slices with no tumor region presented in the ground truth are excluded from the dataset in our experiments, after which we resize them to 256×256 and then add 25% negative samples to each dataset for data balance. In total, our experiments comprise 32,158 pairs of PET/CT slices from

the Hecktor dataset and 29,065 pairs of PET/CT slices from the AutoPET dataset. We conduct 5-fold cross-validation, where each dataset is randomly partitioned into 5 mutually exclusive subsets based on different patients, so as to ensure that different subsets do not contain slices of the same patients. The algorithm is then run five rounds, in each of which one of the five subsets is used as the test set, one is used as the validation set while the left three are employed as the training set. Finally, the average results of five experiments on the test sets are used to evaluate the segmentation performance of the method.

4.2. Implementation details and metrics

The proposed approach is implemented using Python and the PyTorch (Paszke et al., 2019) library on a PC equipped with an NVIDIA GTX 3090 GPU (24 GB memory). The training is conducted using the Adam optimizer with a momentum of 0.99. Based on empirical observations, the learning rate is set to 1×10^{-4} and the number of iterations is set to 100. By training the model with different hyperparameters and evaluating it on the validation set, the hyperparameter λ_1 in Eq. (5) is manually adjusted to 100.0.

The segmentation model’s performance is evaluated in terms of the Dice similarity coefficient (DSC) in Eq. (21), Jaccard in Eq. (22), 95% Hausdorff Distance (HD95) in Eq. (23), sensitivity (Sens) in Eq. (24) and precision (Pre) in Eq. (25),

$$DSC(X, Y) = \frac{2|X \cap Y|}{|X| + |Y|} \quad (21)$$

$$Jaccard(X, Y) = \frac{|X \cap Y|}{|X \cup Y|} \quad (22)$$

$$HD95(X, Y) = 0.95 \max \left\{ \sup_{x \in X} \inf_{y \in Y} E_d(x, y), \sup_{y \in Y} \inf_{x \in X} E_d(x, y) \right\} \quad (23)$$

$$Sens = \frac{TP}{TP + FN} \quad (24)$$

$$Pre = \frac{TP}{TP + FP} \quad (25)$$

where X represents the predicted output of the network and Y represents the ground truth labels, E_d is the euclidean distance between points x and y , sup and inf are supremum and infimum, TP (true positives) represents the number of positive samples correctly classified as positive, FP (false positives) is the number of negative samples incorrectly classified as positive and FN (false negatives) represents the number of positive samples incorrectly classified as negative.

The Dice coefficient evaluates the similarity between the predicted labels and the ground truth by calculating the ratio of the overlapping regions. A Dice value closer to 1 indicates

a higher similarity between the model prediction and the segmentation ground truth, indicating a better segmentation performance. Similarly, Jaccard is also used to measure the similarity and dissimilarity between the model output and the segmentation ground truth. A higher Jaccard value indicates better segmentation performance.

The Hausdorff distance is a measure used to quantify the distance between two sets, which computes the maximum shortest distance from any point in one set to the other set. The Euclidean distance is typically employed as the distance metric. The 95% Hausdorff Distance (95HD) refers to the maximum distance among the sorted Hausdorff distances between the point pairs of the predicted labels and the ground truth, considering only the top 95% of these distances. 95HD is commonly used to evaluate the local accuracy of predicted labels, where a smaller Hausdorff distance value indicates better segmentation results. Sensitivity measures the proportion of positives correctly identified and Precision measures the proportion of true positive pixels in the predictions.

4.3. Comparisons with the state-of-the-art methods

We conducted comparative segmentation experiments on both the AutoPET and Hecktor datasets. Six most recent multimodal tumor segmentation methods, namely CML (Zhang et al., 2021), MMEF (Huang et al., 2021a), ADNet (Peng and Sun, 2023), AATSN (Ahmad et al., 2023), MFCNet (Wang et al., 2023) and CSCA (Shu et al., 2024), are compared, whose results are shown in Table 1.

On the AutoPET dataset, AATSN (Ahmad et al., 2023) performs the worst among others. This may be due to its poor capability in capturing the regions of interest with its lightweight attention mechanism. As compared with the AATSN, CML (Zhang et al., 2021) achieved an improved performance with a DSC score of 78.88%. This can be attributed to the introduction of the cross-modality Feature Transition Module to reduce the domain gap between PET and CT before segmentation. MFCNet (Wang et al., 2023) further improves the DSC score to 79.35% by integrating a calibration network but sacrifices the accuracy of tumor edges as indicated by the increased HD95 compared to CML (Zhang et al., 2021) (by 0.46mm). ADNet (Peng and Sun, 2023) achieves high DSC score and precision (80.30% and 85.26%, respectively) by learning multimodal features through channel feature separation. Upon utilizing the Dempster-Shafer Theory for feature fusion strategy, MMEF (Huang et al., 2021a) achieves the third best sensitivity of 85.46% among all methods. CSCA (Shu et al., 2024) has the highest sensitivity of 88.52% due to its channel and space compound attention. It is worth noting that although our MEFN ranks secondly in sensitivity, it outperforms all other models in terms of metrics except the sensitivity. It achieves 82.45% in DSC, 75.32% in Jaccard, 2.96mm in HD95, 86.23% in sensitivity and 88.55% in precision. Specifically, the DSC score is improved by 2.15% compared to the second-best model, ADNet.

On the Hecktor dataset, due to its multi-task nature of the dataset, feature separation struggles to differentiate tumor features from different tasks, resulting in poor performance of AD-

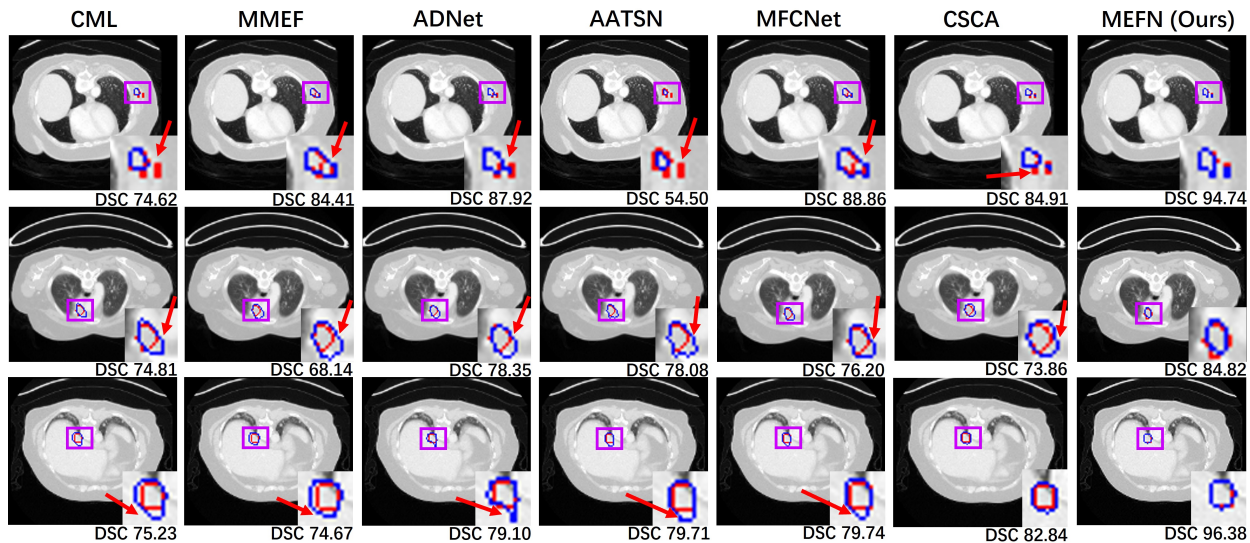


Fig. 4. Segmentation results (blue contour) from different multi-modal segmentation methods of three sample images for three patients from the AutoPET dataset. The ground truth is displayed in red contour. Each row represents segmentation results for the same patient. The bottom right corner of each image displays the enlarged version of the region indicated by the purple box. Red arrows highlight the mis-segmented regions.

Table 1

Segmentation performance of MEFN and other state-of-the-art methods on AutoPET and Hecktor datasets (Mean \pm std). The best results are highlighted in bold and the second-best ones are underlined.

Dataset	Methods	DSC(%)	Jaccard(%)	HD95(mm)	Sens(%)	Pre(%)
AutoPET	CML (Zhang et al., 2021)	78.88 \pm 27.18	71.25 \pm 27.83	3.62 \pm 12.26	84.00 \pm 21.29	83.73 \pm 25.41
	MMEF (Huang et al., 2021a)	78.70 \pm 27.81	71.24 \pm 28.26	3.91 \pm 9.03	85.46 \pm 21.25	82.27 \pm 25.90
	ADNet (Peng and Sun, 2023)	<u>80.30 \pm 28.15</u>	<u>73.72 \pm 28.77</u>	<u>3.46 \pm 8.61</u>	85.68 \pm 22.07	<u>85.26 \pm 25.00</u>
	AATSN (Ahmad et al., 2023)	69.28 \pm 32.94	61.10 \pm 32.76	7.29 \pm 14.76	75.11 \pm 32.77	80.12 \pm 26.14
	MFCNet (Wang et al., 2023)	79.35 \pm 21.63	70.54 \pm 27.16	4.08 \pm 9.26	84.62 \pm 22.86	84.41 \pm 26.18
	CSCA (Shu et al., 2024)	78.71 \pm 27.52	71.17 \pm 28.26	4.09 \pm 9.48	88.52 \pm 21.72	78.76 \pm 26.15
	MEFN (Ours)	82.45 \pm 13.21	75.32 \pm 27.26	2.96 \pm 7.75	<u>86.23 \pm 20.55</u>	88.55 \pm 23.63
Hecktor	CML (Zhang et al., 2021)	<u>80.12 \pm 25.32</u>	63.27 \pm 27.59	4.26 \pm 7.21	76.73 \pm 33.74	86.32 \pm 19.61
	MMEF (Huang et al., 2021a)	78.11 \pm 23.95	61.11 \pm 28.63	<u>4.16 \pm 7.02</u>	69.09 \pm 32.14	86.80 \pm 17.48
	ADNet (Peng and Sun, 2023)	73.97 \pm 28.96	64.02 \pm 33.53	10.72 \pm 19.72	71.53 \pm 34.28	81.49 \pm 26.86
	AATSN (Ahmad et al., 2023)	76.73 \pm 25.21	<u>65.13 \pm 26.91</u>	12.24 \pm 20.85	<u>78.31 \pm 27.58</u>	79.43 \pm 23.13
	MFCNet (Wang et al., 2023)	74.14 \pm 27.72	62.96 \pm 22.41	6.41 \pm 7.01	77.20 \pm 27.13	76.12 \pm 28.85
	CSCA (Shu et al., 2024)	77.13 \pm 21.41	60.21 \pm 24.86	4.39 \pm 7.06	79.37 \pm 28.82	74.79 \pm 21.30
	MEFN (Ours)	83.35 \pm 23.09	71.73 \pm 28.02	3.27 \pm 7.21	78.03 \pm 29.47	90.06 \pm 16.07

Net (Peng and Sun, 2023), although it performs well on the AutoPET dataset. AATSN (Ahmad et al., 2023) performs well due to its lightweight attention mechanism, achieving a DSC score of 76.73% and ranking the second in Jaccard (65.13%). Additionally, CML (Zhang et al., 2021) achieves high DSC score and precision (80.12% and 86.32%, respectively) due to its unique multi-modal feature fusion mechanism. CSCA (Shu et al., 2024) also achieves the highest sensitivity of 79.37% due to its channel and space compound attention. Notably, our MEFN outperforms other segmentation networks significantly in terms of DSC, Jaccard, HD95, sensitivity and precision, which reaches 83.35%, 71.73%, 3.27mm, 78.03% and 90.06%, respectively. Specifically, as compared with the second-best network, our MEFN improves the DSC score and precision by 3.23% and 3.26%, respectively.

Besides the aforementioned quantitative comparisons among

different methods, visual assessments and comparisons are also conducted between MEFN and other state-of-the-art multi-modal tumor segmentation methods. Fig. 4 gives the segmented results from different methods for three different CT sample images of patients from AutoPET dataset where blue contour gives the predicted tumor region while red contour gives the ground truth. Fig. 5 gives the segmentation results for three CT sample images of three patients from the Hecktor dataset where blue and yellow contours give the predicted regions for GTVp and GTVn tumors while red and green contours give the ground truths for these two kinds of tumors, respectively. Tumor regions marked with purple boxes are enlarged and placed on the right bottom of each sample image. Red arrows point out the mis-segmented tumor regions in each sample image. From Fig. 4, it can be seen that for small tumors throughout the body, such as in the first patient, CML (Zhang et al., 2021) and

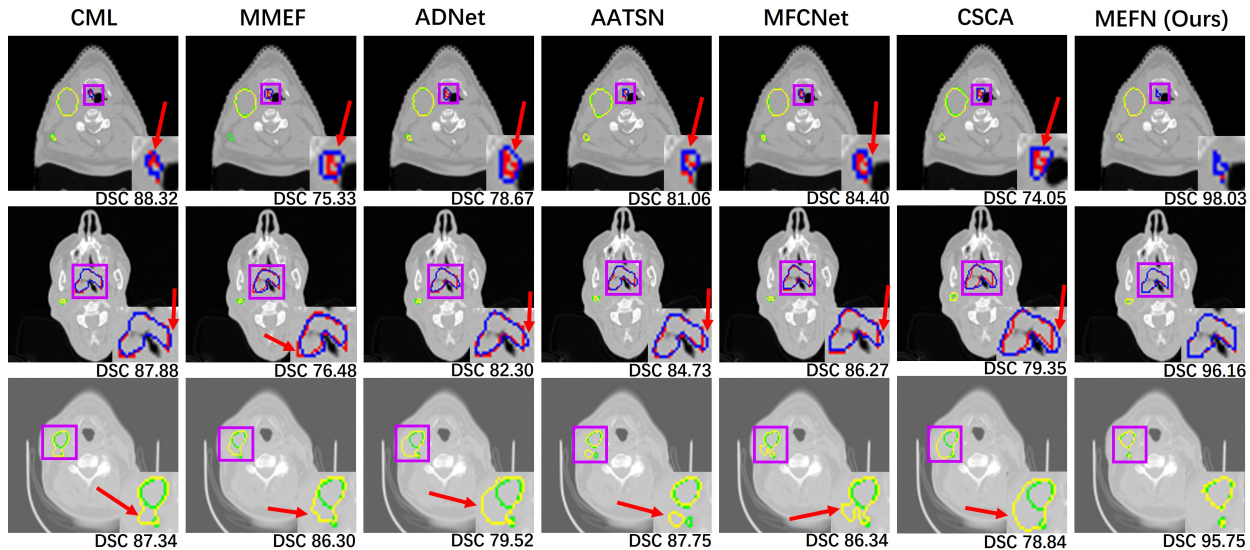


Fig. 5. Segmentation results from different multi-modal segmentation methods of three sample images for different patients on the Hecktor dataset. Blue and yellow contours represent the segmentation results of the GTVp and GTVn tasks, respectively. Red and green contours represent the ground truth of the GTVp and GTVn tasks, respectively. Each row represents the segmentation results of the same patient. The bottom right corner of each image displays the enlarged version of region indicated by the purple box. Red arrows highlight the mis-segmented regions.

AATSN (Ahmad et al., 2023) lead to under segmented results, while MMEF (Huang et al., 2021a) and MFCNet (Wang et al., 2023) tend to merge two separate tumors into one large tumor. Although CSCA (Shu et al., 2024) can segment all tumors, it fails to delineate the tumor edges accurately. Additionally, for the second and third patients, the segmentation results of other models also differ in shape from the ground truth and exhibit many redundant edges. In contrast, our MEFN not only effectively segments all small tumors but also achieves the highest accuracy in fitting the tumor edges. It can also be seen in Fig. 5 that most methods fail to accurately distinguish tumorous and normal tissues in boundary regions, which results in redundant or missing tumor edges such as in the segmentation results of the first and second patients. Furthermore, for regions with adjacent tumors, such as in the third patient, AATSN (Ahmad et al., 2023) cannot accurately locate and segment small tumors, while other methods tend to segment two separate tumors into one larger tumor. In comparison, our method can precisely locate each tumor and capture subtle differences between tumors, yielding better segmentation results. These results indicate that our proposed MEFN achieves more accurate segmentation masks and more precise tumor edges compared to other methods.

4.4. Ablative study

4.4.1. Effectiveness of each component

To better perform multi-modal segmentation, DBTF, MTGA and DFC modules were incorporated in our segmentation model. To validate the effectiveness of each component, ablation experiments are conducted. The baseline network for comparison is the UNet without the DBTF, MTGA and DFC modules. In Baseline, PET features and CT features are fused simply by concatenation and input to Dec_f to obtain the final result. The

Baseline+DBTF is the one by incorporating the DBTF module to the Baseline model. The Baseline+DBTF+MTGA is the model by further incorporating MTGA to Baseline+DBTF. The Baseline+DBTF+DFC denotes the model by incorporating DFC to Baseline+DBTF. Finally, upon incorporating all three components into the Baseline we obtain our proposed MEFN. Ablative experiments were conducted respectively on the AutoPET and Hecktor datasets whose results are shown in Table 2. From this table, it can be observed that on the AutoPET dataset, the result of Baseline+DBTF is significantly superior to that of the Baseline model (81.63% vs. 79.91% in DSC), which indicates that the DBTF module effectively utilizes the uncertainties of PET features, CT features and fused features to achieve more reasonable fusion of segmentation results. After incorporating MTGA, the model achieves a noticeable improvement in HD95 and sensitivity, which indicates that MTGA can effectively assist the network in Tumor-Related initialization and hence aids in identifying more whole-body tumors. With the introduction of DFC, the result is also improved compared to Baseline+DBTF (82.43% vs. 81.63% in DSC), demonstrating that the proposed feature fusion module effectively eliminates redundant features and improves segmentation performance. After incorporating all components, further improvements can be observed, which indicates that all modules contribute corporatively to the proposed method.

4.4.2. Effectiveness of Uncertainty Calibrator

In this work, the Uncertainty Calibrator (UC) is proposed to achieve semantic correction of decoder features during feature fusion. To validate the effectiveness of the proposed method, we introduced perturbations of Gaussian noise at different levels (with noise variance $\sigma^2 = 0.1, 0.2, 0.3$) and patch-size random masking (mask ratio $\gamma = 0.04, 0.08$) into the AutoPET and

Table 2

Effectiveness of each component on AutoPET and Hecktor datasets (Mean \pm std). The best results are highlighted in bold and the second-best ones are underlined.

Dataset	Methods	DBTF	MTGA	DFC	DSC(%)	Jaccard(%)	HD95(mm)	Sens(%)	Pre(%)
AutoPET	Baseline	-	-	-	79.91 \pm 27.72	73.86 \pm 31.51	3.50 \pm 10.29	80.26 \pm 24.27	87.31 \pm 23.82
	Baseline+DBTF	✓	-	-	81.63 \pm 25.17	74.43 \pm 26.31	4.68 \pm 10.81	83.31 \pm 22.41	<u>88.18 \pm 20.59</u>
	Baseline+DBTF+MTGA	✓	✓	-	82.29 \pm 25.46	75.22 \pm 26.45	3.05 \pm 7.91	<u>86.17 \pm 19.95</u>	86.29 \pm 22.79
	Baseline+DBTF+DFC	✓	-	✓	82.43 \pm 24.29	75.28 \pm 25.64	3.05 \pm 7.91	85.07 \pm 21.16	87.33 \pm 20.71
	MEFN (Ours)	✓	✓	✓	82.45 \pm 13.21	75.32 \pm 27.26	2.96 \pm 7.75	86.23 \pm 20.55	88.55 \pm 23.63
Hecktor	Baseline	-	-	-	81.42 \pm 31.21	69.07 \pm 32.24	3.68 \pm 7.27	72.32 \pm 27.75	89.31 \pm 32.65
	Baseline+DBTF	✓	-	-	81.63 \pm 25.71	71.22 \pm 29.30	3.52 \pm 7.09	<u>77.19 \pm 30.92</u>	89.43 \pm 15.84
	Baseline+DBTF+MTGA	✓	✓	-	82.45 \pm 23.02	69.49 \pm 28.60	3.62 \pm 7.32	74.38 \pm 30.03	<u>89.67 \pm 15.63</u>
	Baseline+DBTF+DFC	✓	-	✓	<u>83.13 \pm 23.55</u>	<u>71.44 \pm 26.31</u>	<u>3.34 \pm 8.29</u>	73.31 \pm 22.41	88.18 \pm 20.59
	MEFN (Ours)	✓	✓	✓	83.35 \pm 23.09	71.73 \pm 28.02	3.27 \pm 7.21	78.03 \pm 29.47	90.06 \pm 16.07

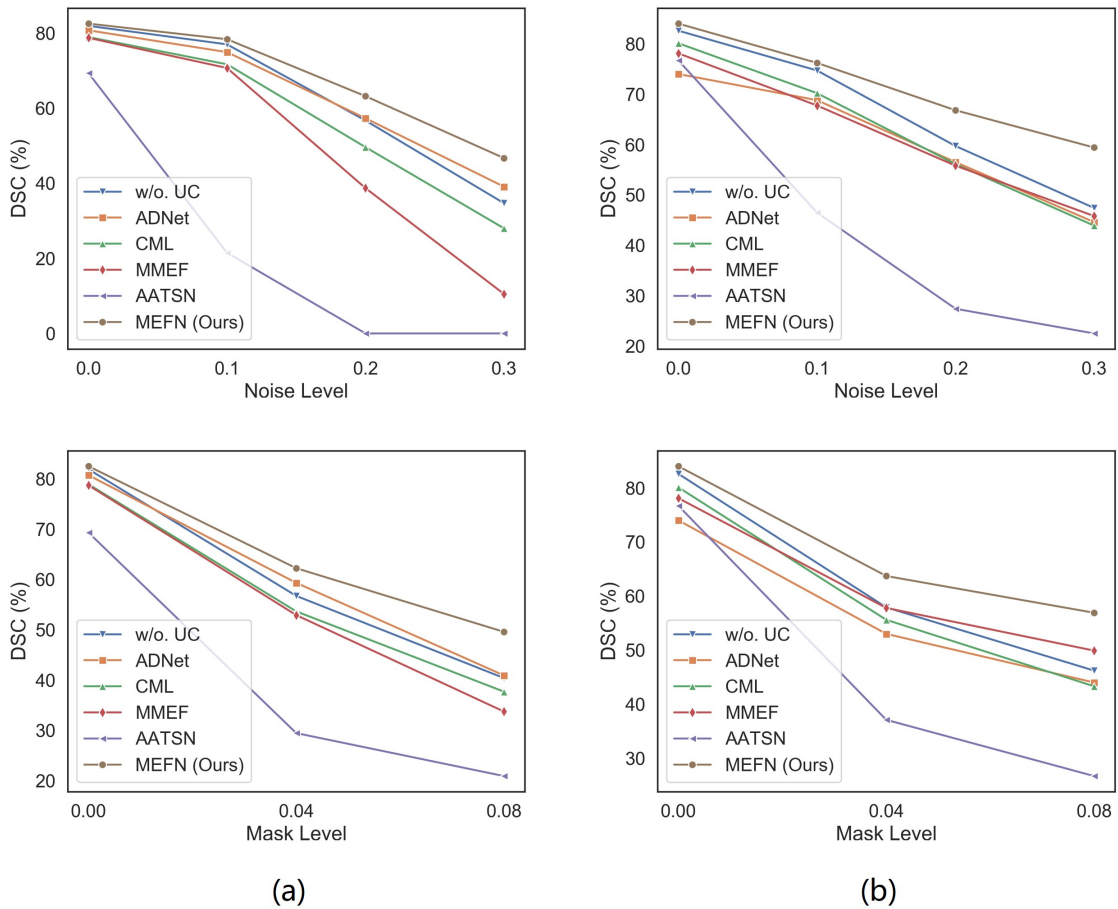


Fig. 6. The performance of MEFN, MEFN without UC (w/o. UC) and other multi-modal segmentation models on two datasets with different levels of Gaussian noise perturbations and patch-size random masking: (a) AutoPET Dataset, (b) Hecktor Dataset.

Hecktor datasets, respectively. For patch-size random masking, we use 3×3 black boxes to cover the original input image with a uniform distribution, and the mask ratio γ represents the proportion of black boxes to the total number of pixels. We compare the performance of our MEFN, MEFN without UC (referred to as w/o. UC) and other models on out-of-distribution data (with large uncertainty), whose results are shown in Fig. 6. From

this figure, it can be observed that as the perturbation level increases, the performance of other models deteriorate drastically, while our proposed MEFN performs much more robust to random noise and random masking. We notice that after removing UC, the performance degradation rate of our model without UC is comparable to CML (Zhang et al., 2021) (blue line and green line), which indicates that the model loses the ability to

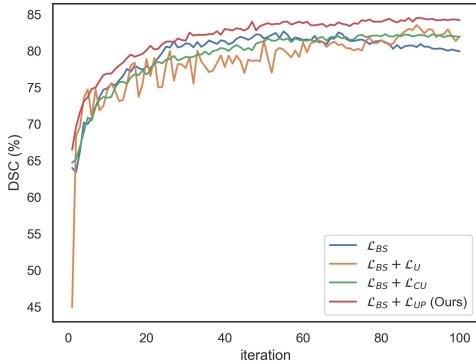


Fig. 7. The DSC of MEFN during its training process under different loss functions on the test set of Hecktor dataset.

calibrate semantic features in large uncertainty regions after removing UC from our MEFN model.

4.4.3. Effectiveness of Uncertainty Perceptual Loss

In our work, the Uncertainty Perceptual Loss (\mathcal{L}_{UP}) is proposed to provide supervision for uncertainty. To validate the effectiveness of \mathcal{L}_{UP} in model training, we compare performance of three models trained respectively under the combination of the baseline loss and other three different loss functions used for supervising uncertainty: uncertainty loss (Huang et al., 2021b) (\mathcal{L}_U), calibrated uncertainty loss (Zou et al., 2023) (\mathcal{L}_{CU}) and a variant of calibrated uncertainty loss (Zou et al., 2023) ($\mathcal{L}_{CU}(dis)$). Table 3 gives the segmentation performance of models trained under different loss functions. On the AutoPET dataset, compared to the model trained under the baseline loss \mathcal{L}_{BS} , models trained under $\mathcal{L}_{BS} + \mathcal{L}_U$ (Huang et al., 2021b), $\mathcal{L}_{BS} + \mathcal{L}_{CU}$ (Zou et al., 2023) or $\mathcal{L}_{BS} + \mathcal{L}_{CU}(dis)$ (Zou et al., 2023) yield slight improvements in segmentation performance (77.92% vs. 78.65% vs. 77.93% vs. 78.46% in DSC). Specifically, when incorporating our proposed Uncertainty Perceptual Loss, the overall segmentation performance is significantly improved compared to that of the one trained under the baseline loss \mathcal{L}_{BS} (77.92% vs. 82.45% in DSC). On the Hecktor dataset, although the model trained under $\mathcal{L}_{BS} + \mathcal{L}_{UP}$ does not perform the best in terms of HD95 and precision, there is still a substantial improvement in overall metrics compared to the one trained under the baseline loss \mathcal{L}_{BS} . Fig. 7 illustrates changes in DSC with iterations during the training processes of models under different loss functions. It can be observed from Fig. 7 that the DSC of the model trained under \mathcal{L}_{BS} shows a decreasing trend with increased iterations, indicating overfitting. After incorporating \mathcal{L}_{UP} to the loss function, not only does the overall segmentation performance improve, but the overfitting problem in the later training stages is also alleviated. With the incorporation of \mathcal{L}_U (Huang et al., 2021b), the model exhibits strong oscillations in the early training stages, which is possibly due to inaccurate quantification of uncertainty by the model in initial stages. However, upon introducing an annealing factor β_t , our proposed \mathcal{L}_{UP} stabilizes the early training of the model.

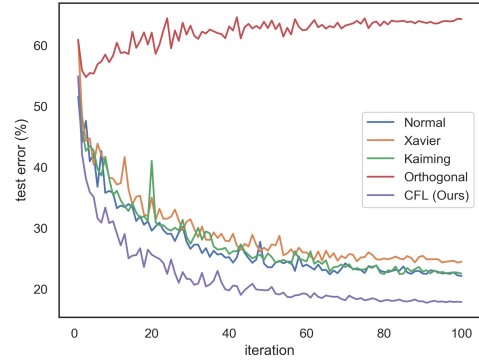


Fig. 8. Test error of MEFN during its training process with different initialization schemes on the test set of AutoPET dataset.

4.4.4. Effectiveness of CFL

In our work, a novel task-driven initialization module called CFL is introduced for multi-modal segmentation tasks. Here, the effectiveness of such an initialization method for multi-modal segmentation is evaluated in terms of the test error defined as follows:

$$error = 1 - \frac{TP + TN}{TP + TN + FP + FN} \quad (26)$$

where TP , FP and FN are as defined in Section 4.2, TN (true negatives) represents the number of negative samples correctly classified as negative. We compare four different initialization methods in terms of test error curves during model training. These four initialization methods considered are Normal (standard normal distribution), Xavier (Glorot and Bengio, 2010), Kaiming (He et al., 2015) and Orthogonal (Ahmad et al., 2023). Fig. 8 illustrates curves of the test error on the AutoPET dataset, while Table 4 provides the final test error for both AutoPET and Hecktor datasets.

As a baseline, the Normal initialization strategy achieves final test errors of 22.13% and 17.72% on the AutoPET and Hecktor datasets, respectively. When using CFL initialization method, test error on the same dataset are reduced to 17.62% and 15.76%, respectively, which demonstrates a significant improvement. Conversely, other initialization methods show minor improvements or even performance degradation. From the Fig. 8, it can be clearly seen that when using Orthogonal (Saxe et al., 2013) initialization method, the model have fallen into a local optimum, resulting in poor generalization performance. It is evident that curves for the test error when utilizing the CFL initialization method are notably lower than those with other initialization methods and exhibit smoother trends. These results convincingly demonstrate the effectiveness of CFL.

4.5. Visual assessment on segmentation uncertainty

Intuitively, the uncertainty output from different models should be positively correlated to data perturbation (i.e., the output uncertainty should increase with the increment of perturbation levels of input data). The conservation of such a positive correlation is a measure of the confidential level of the

Table 3

The performance of MEFN trained under different loss functions on AutoPET and Hecktor datasets (Mean \pm std). The best results are highlighted in bold and the second-best ones are underlined.

Dataset	Methods	DSC(%)	Jaccard(%)	HD95(mm)	Sens(%)	Pre(%)
AutoPET	\mathcal{L}_{BS}	77.92 \pm 31.45	71.56 \pm 31.25	3.31 \pm 7.55	83.96 \pm 24.28	84.94 \pm 26.28
	$\mathcal{L}_{BS} + \mathcal{L}_U$ (Huang et al., 2021b)	<u>78.65 \pm 31.27</u>	<u>75.19 \pm 31.76</u>	<u>3.06 \pm 7.83</u>	<u>84.94 \pm 31.42</u>	<u>87.76 \pm 17.82</u>
	$\mathcal{L}_{BS} + \mathcal{L}_{CU}$ (Zou et al., 2023)	77.93 \pm 30.14	71.23 \pm 30.69	3.49 \pm 7.91	82.92 \pm 25.17	85.26 \pm 24.27
	$\mathcal{L}_{BS} + \mathcal{L}_{CU}(dis)$ (Zou et al., 2023)	78.46 \pm 30.26	72.06 \pm 31.72	3.46 \pm 7.90	83.73 \pm 26.42	85.46 \pm 25.91
	$\mathcal{L}_{BS} + \mathcal{L}_{UP}$ (Ours)	82.45 \pm 13.21	75.32 \pm 27.26	2.96 \pm 7.75	86.23 \pm 20.55	88.55 \pm 23.63
Hecktor	\mathcal{L}_{BS}	81.46 \pm 26.17	65.65 \pm 33.23	4.39 \pm 9.14	69.47 \pm 35.09	91.06 \pm 19.40
	$\mathcal{L}_{BS} + \mathcal{L}_U$ (Huang et al., 2021b)	<u>83.03 \pm 23.17</u>	<u>70.40 \pm 34.21</u>	<u>3.20 \pm 7.83</u>	<u>72.13 \pm 34.32</u>	<u>92.19 \pm 19.17</u>
	$\mathcal{L}_{BS} + \mathcal{L}_{CU}$ (Zou et al., 2023)	82.44 \pm 25.71	69.76 \pm 33.20	3.19 \pm 7.92	<u>72.96 \pm 34.61</u>	92.92 \pm 16.12
	$\mathcal{L}_{BS} + \mathcal{L}_{CU}(dis)$ (Zou et al., 2023)	79.87 \pm 31.91	51.61 \pm 42.85	4.64 \pm 8.35	52.46 \pm 43.17	91.80 \pm 19.46
	$\mathcal{L}_{BS} + \mathcal{L}_{UP}$ (Ours)	83.35 \pm 23.09	71.73 \pm 28.02	3.27 \pm 7.21	78.03 \pm 29.47	90.06 \pm 16.07

Table 4

Final test error (%) with different initialization schemes (Mean \pm std). The best results are highlighted in bold and the second-best ones are underlined.

Type	AutoPET	Hecktor
Normal	22.13 \pm 27.45	17.72 \pm 15.19
Xavier (Glorot and Bengio, 2010)	24.31 \pm 23.17	17.91 \pm 28.71
Kaiming (He et al., 2015)	22.55 \pm 29.17	19.36 \pm 21.24
Orthogonal (Saxe et al., 2013)	54.86 \pm 47.17	17.56 \pm 26.90
CFL (Ours)	17.62 \pm 18.51	15.76 \pm 12.67

output uncertainty of different models. Thus, we introduce perturbation of different levels into the dataset with the same perturbation methods as described in Section 4.4.2 and then conduct segmentation with different models. The correlation of the output uncertainty with the level of perturbation is employed to assess the reliability of the output uncertainty. We visually compare the uncertainty output from the DBTF module of our MEFN with that output from MMEF (Huang et al., 2021a) for the segmentation results. Fig. 9 gives the segmentation results of two sample images from the AutoPET dataset along with their segmentation uncertainty. The top part of this figure correspond to the first sample while the bottom part correspond to the second sample, with columns from left to right corresponding to sample CT image, sample PET image, ground truth label, segmentation results from the MMEF and their uncertainty, segmentation results from our MEFN and their uncertainty. Rows of this figure correspond to the sample images themselves and and their perturbed versions. Tumor regions are marked with red boxes. It can be evidently seen from the 4th and 6th columns of both samples that the segmentation results from both models become inferiors to different extent as the level of perturbation and the degree of Out-Of-Distribution (OOD) data increase. Concurrently, the uncertainty predicted by our MEFN also consistently increases (as shown in the 7th columns in both samples), which implies a positive correlation between the uncertainty and the level of perturbation. In contrast, the uncertainty predicted with MMEF (Huang et al., 2021a) inconsistently decreases (as shown in the 5th columns in both samples) in some cases, which obviously violates the positive correlation requirement and is probably due to over-

confidence in the model. These observations indicate that our proposed MEFN avoids blind confidence and provides radiologists and doctors with more credible uncertainty of the segmentation results. Moreover, beside tumor regions, MMEF (Huang et al., 2021a) exhibits significant uncertainty in non-tumor regions (as pointed by red arrows in the uncertainty images in the third row in the first sample and first, seconde and third rows in the second sample). In contrast, MEFN only shows uncertainty in tumor regions(as shown in the 7th columns in both samples), indicating precise localization ability for tumors and more accurate handling of uncertainty in non-tumor regions. Furthermore, as shown in the 5th and 7th columns of the first rows in both samples, our MEFN shows less uncertainty as compared with MMEF (Huang et al., 2021a), which indicates that our MEFN can provide more reliable segmentation results.

Besides, it can be observed from the last rows for both sample images that although the proposed method may not segment tumor regions well for OOD data, it provides high uncertainty values in areas where tumors may exist, which prompts doctors performing further manual inspection of the tumorous regions. This can greatly boost doctors' confidence in trusting the model during clinical diagnosis, breaking the awkward situation of being hesitant to use deep learning due to its black-box nature.

5. Conclusion

This paper proposes a novel multi-modal Evidential fusion network for PET/CT tumor segmentation. The motivation of this work is to develop a method that can fuse the somewhat inconsistent functional and anatomical information for joint segmentation of tumors in both the CT and PET images. In this method, a Generative Adversarial Network-based Cross-modality Feature Learning module is first designed to obtain task-driven initialization of network parameters by reducing the domain gap. Then, two U-Net networks are utilized to extract CT and PET features for feature fusion, during which a Dual-attention Calibrating module is specifically designed to reduce the impact of redundancy and confliction between features of different modalities on segmentation tasks. Finally, the output results are trustworthily fused based on the Dempster-Shafer Theory according to uncertainty. Extensive experiments were

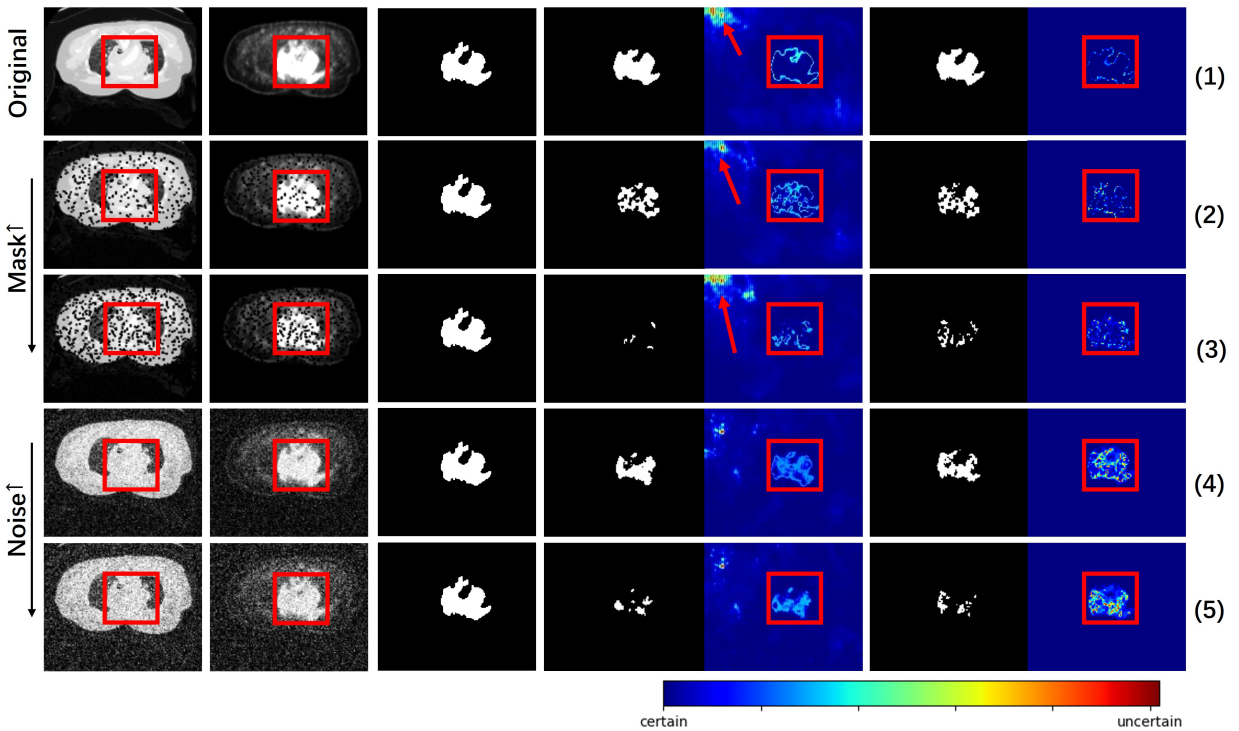
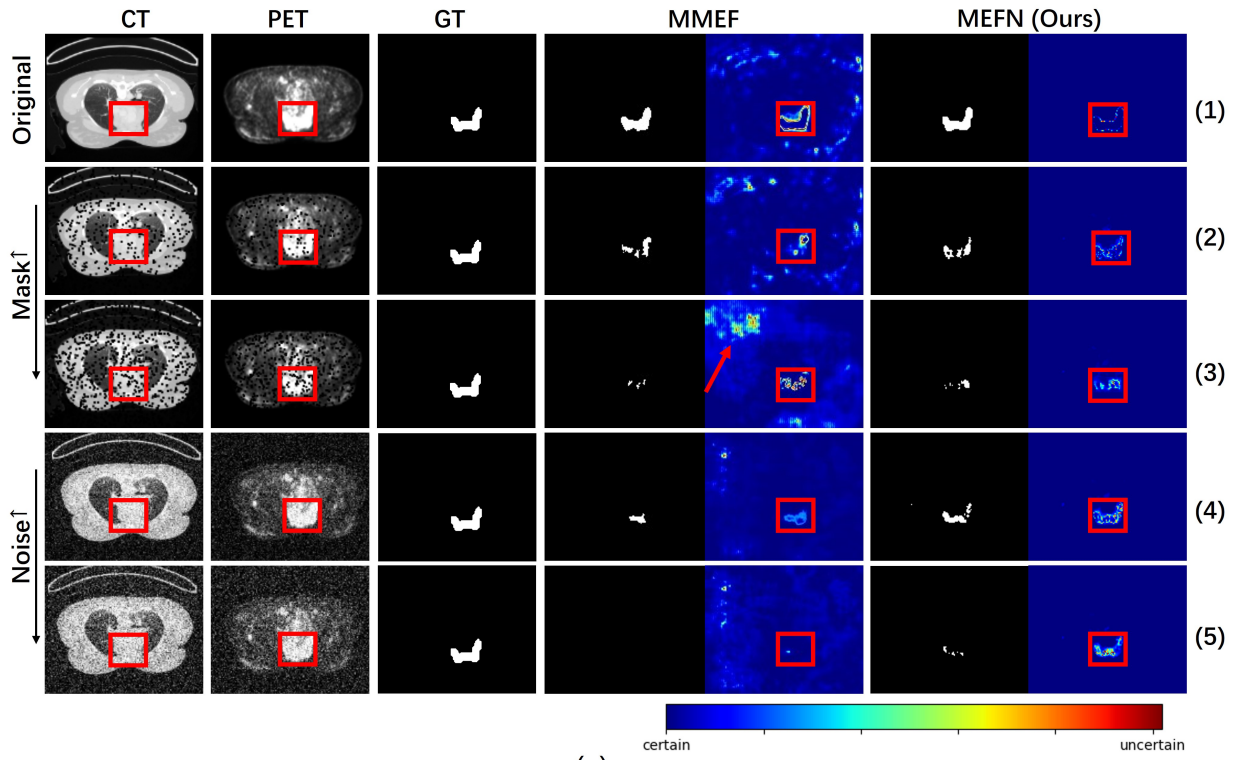


Fig. 9. Segmentation results and their uncertainty for two sample images from the AutoPET dataset. Each row corresponds to the results for the sample image or for their perturbed versions (with Gaussian noise ($\sigma^2 = 0.2, 0.3$) or patch-size random masked ($\gamma = 0.04, 0.08$)). The columns correspond from left to right to sample CT image, sample PET image, ground truth labels, segmentation results and their uncertainty from MMEF and our MEFN, respectively.

performed on two publicly available datasets whose results demonstrate the superiority of the proposed MEFN method over other state-of-the-art multi-modal image segmentation methods. The improvements achieved with our MEFN method over other state-of-the-art methods in PET/CT multi-modal tumor segmentation amount to 2.15% and 3.23% in DSC on the AutoPET dataset and the Hecktor dataset, respectively.

A limitation of this work is that it is an end-to-end network model, resulting in large amount of model parameters and long training time. In future work, we will focus on deriving lightweight version of this network model or use two-stage training scheme to reduce network parameters while maintaining performance, making it more applicable in real clinical scenarios.

CRedit authorship contribution statement

Yuxuan Qi: Conceptualization, Writing - review and editing, Writing - original draft, Visualization, Software, Methodology, Investigation, Data curation, Formal Analysis. **Li Lin:** Conceptualization, Writing - review and editing, Methodology, Investigation, Supervision, Validation, Formal Analysis. **Jingya Zhang:** Resource, Data curation, Funding acquisition. **Jiajun Wang:** Conceptualization, Writing - review and editing, Validation, Supervision, Project administration, Funding acquisition, Conceptualization. **Bin Zhang:** Resource, Investigation, Data curation, Funding acquisition.

Declaration of competing interest

The authors declare that they have no known competing financial interests or personal relationships that could have appeared to influence the work reported in this paper.

Data availability

Data will be made available on request.

Acknowledgments

This work is supported by the National Natural Science Foundation of China, No. 60871086 and No. 61473243, the Natural Science Foundation of Jiangsu Province China, No. BK2008159 and the Natural Science Foundation of Suzhou No. SYG201113. The authors thank the anonymous reviewers for their constructive comments and valuable suggestions.

References

Ahmad, I., Xia, Y., Cui, H., Islam, Z.U., 2023. Aatsn: Anatomy aware tumor segmentation network for pet-ct volumes and images using a lightweight fusion-attention mechanism. *Computers in Biology and Medicine* 157, 106748. URL: <https://www.sciencedirect.com/science/article/pii/S0010482523002135>, doi:<https://doi.org/10.1016/j.combiomed.2023.106748>.

Begoli, E., Bhattacharya, T., Kusnezov, D., 2019. The need for uncertainty quantification in machine-assisted medical decision making. *Nature Machine Intelligence* 1, 20–23. URL: <https://doi.org/10.1038/s42256-018-0004-1>, doi:[10.1038/s42256-018-0004-1](https://doi.org/10.1038/s42256-018-0004-1).

Ben-Cohen, A., Klang, E., Raskin, S.P., Soffer, S., Ben-Haim, S., Konen, E., Amitai, M.M., Greenspan, H., 2019. Cross-modality synthesis from ct to pet using fcnet and gan networks for improved automated lesion detection. *Engineering Applications of Artificial Intelligence* 78, 186–194. URL: <https://www.sciencedirect.com/science/article/pii/S0952197618302513>, doi:<https://doi.org/10.1016/j.engappai.2018.11.013>.

Bi, L., Kim, J., Kumar, A., Feng, D., Fulham, M., 2017. Synthesis of positron emission tomography (pet) images via multi-channel generative adversarial networks (gans), in: *Molecular Imaging, Reconstruction and Analysis of Moving Body Organs, and Stroke Imaging and Treatment: Fifth International Workshop, CMMI 2017, Second International Workshop, RAMBO 2017, and First International Workshop, SWITCH 2017, Held in Conjunction with MICCAI 2017, Québec City, QC, Canada, September 14, 2017, Proceedings 5*, Springer. pp. 43–51.

Bowles, C., Chen, L., Guerrero, R., Bentley, P., Gunn, R., Hammers, A., Dickie, D.A., Hernández, M.V., Wardlaw, J., Rueckert, D., 2018. Gan augmentation: Augmenting training data using generative adversarial networks. *arXiv preprint arXiv:1810.10863* URL: <https://api.semanticscholar.org/CorpusID:53024682>.

Chen, H., Dou, Q., Yu, L., Qin, J., Heng, P.A., 2018. Voxresnet: Deep voxelwise residual networks for brain segmentation from 3d mr images. *NeuroImage* 170, 446–455. URL: <https://www.sciencedirect.com/science/article/pii/S1053811917303348>, doi:<https://doi.org/10.1016/j.neuroimage.2017.04.041>.

Fu, X., Bi, L., Kumar, A., Fulham, M., Kim, J., 2021. Multimodal spatial attention module for targeting multimodal pet-ct lung tumor segmentation. *IEEE Journal of Biomedical and Health Informatics* 25, 3507–3516. URL: <https://ieeexplore.ieee.org/abstract/document/9354983>, doi:[10.1109/JBHI.2021.3059453](https://doi.org/10.1109/JBHI.2021.3059453).

Gal, Y., Ghahramani, Z., 2016. Dropout as a bayesian approximation: Representing model uncertainty in deep learning, in: *international conference on machine learning*, PMLR. pp. 1050–1059. URL: <https://proceedings.mlr.press/v48/gal16.html>.

Gatidis, S., Hepp, T., Früh, M., La Fougère, C., Nikolaou, K., Pfannenber, C., Schölkopf, B., Küstner, T., Cyran, C., Rubin, D., 2022. A whole-body fdg-pet/ct dataset with manually annotated tumor lesions. *Scientific Data* 9, 601. URL: <https://www.nature.com/articles/s41597-022-01718-3>, doi:<https://doi.org/10.1038/s41597-022-01718-3>.

Glorot, X., Bengio, Y., 2010. Understanding the difficulty of training deep feed-forward neural networks, in: *Proceedings of the thirteenth international conference on artificial intelligence and statistics, JMLR Workshop and Conference Proceedings*. pp. 249–256. URL: <https://proceedings.mlr.press/v9/glorot10a.html>.

Goodfellow, I., Pouget-Abadie, J., Mirza, M., Xu, B., Warde-Farley, D., Ozair, S., Courville, A., Bengio, Y., 2020. Generative adversarial networks. *Communications of the ACM* 63, 139–144. URL: <https://doi.org/10.48550/arXiv.1406.2661>.

He, K., Zhang, X., Ren, S., Sun, J., 2015. Delving deep into rectifiers: Surpassing human-level performance on imagenet classification, in: *Proceedings of the IEEE international conference on computer vision*, pp. 1026–1034. URL: https://openaccess.thecvf.com/content_iccv_2015/html/He_Delving_Deep_into_ICCV_2015_paper.html.

Huang, L., Denœux, T., Tonnelet, D., Decazes, P., Ruan, S., 2021a. Deep pet/ct fusion with dempster-shafer theory for lymphoma segmentation, in: *Machine Learning in Medical Imaging: 12th International Workshop, MLMI 2021, Held in Conjunction with MICCAI 2021, Strasbourg, France, September 27, 2021, Proceedings 12*, Springer. pp. 30–39. URL: https://link.springer.com/chapter/10.1007/978-3-030-87589-3_4, doi:https://doi.org/10.1007/978-3-030-87589-3_4.

Huang, L., Ruan, S., Decazes, P., Denœux, T., 2021b. Evidential segmentation of 3d pet/ct images, in: *International conference on belief functions*, Springer. pp. 159–167. URL: https://link.springer.com/chapter/10.1007/978-3-030-88601-1_16.

Huang, L., Ruan, S., Decazes, P., Denœux, T., 2022. Lymphoma segmentation from 3d pet-ct images using a deep evidential net-

work. *International Journal of Approximate Reasoning* 149, 39–60. URL: <https://www.sciencedirect.com/science/article/pii/S0888613X22000962>, doi:<https://doi.org/10.1016/j.ijar.2022.06.007>.

Islam, M.Z., Naqvi, R.A., Haider, A., Kim, H.S., 2023. Deep learning for automatic tumor lesions delineation and prognostic assessment in multi-modality pet/ct: A prospective survey. *Engineering Applications of Artificial Intelligence* 123, 106276. URL: <https://www.sciencedirect.com/science/article/pii/S0952197623004608>, doi:<https://doi.org/10.1016/j.engappai.2023.106276>.

Isola, P., Zhu, J.Y., Zhou, T., Efros, A.A., 2017. Image-to-image translation with conditional adversarial networks, in: *Proceedings of the IEEE conference on computer vision and pattern recognition*, pp. 1125–1134. URL: https://openaccess.thecvf.com/content_cvpr_2017/html/Isola_Image-To-Image_Translation_With_CVPR_2017_paper.html.

Jsang, A., 2018. *Subjective Logic: A formalism for reasoning under uncertainty*. Springer Publishing Company, Incorporated. URL: <https://dl.acm.org/doi/abs/10.5555/3279217>.

Kamnitsas, K., Bai, W., Ferrante, E., McDonagh, S., Sinclair, M., Pawlowski, N., Rajchl, M., Lee, M., Kainz, B., Rueckert, D., et al., 2018. Ensembles of multiple models and architectures for robust brain tumour segmentation, in: *Brainlesion: Glioma, Multiple Sclerosis, Stroke and Traumatic Brain Injuries: Third International Workshop, BrainLes 2017, Held in Conjunction with MICCAI 2017, Quebec City, QC, Canada, September 14, 2017, Revised Selected Papers 3*, Springer. pp. 450–462. URL: https://doi.org/10.1007/978-3-319-75238-9_38.

Kohl, S., Romera-Paredes, B., Meyer, C., De Fauw, J., Ledsam, J.R., Maier-Hein, K., Eslami, S., Jimenez Rezende, D., Ronneberger, O., 2018. A probabilistic u-net for segmentation of ambiguous images. *Advances in neural information processing systems* 31. URL: https://proceedings.neurips.cc/paper_files/paper/2018/file/473447ac58e1cd7e96172575f48dca3b-Paper.pdf.

Lakshminarayanan, B., Pritzel, A., Blundell, C., 2017. Simple and scalable predictive uncertainty estimation using deep ensembles. *Advances in neural information processing systems* 30. URL: https://proceedings.neurips.cc/paper_files/paper/2017/file/9ef2ed4b7fd2c810847ffa5fa85bce38-Paper.pdf.

Li, X., Chen, H., Qi, X., Dou, Q., Fu, C.W., Heng, P.A., 2018. Hdenseunet: Hybrid densely connected unet for liver and tumor segmentation from ct volumes. *IEEE Transactions on Medical Imaging* 37, 2663–2674. URL: <https://ieeexplore.ieee.org/document/8379359>, doi:10.1109/TMI.2018.2845918.

Liu, T., Su, Y., Zhang, J., Wei, T., Xiao, Z., 2021. 3d u-net applied to simple attention module for head and neck tumor segmentation in pet and ct images, in: *3D Head and Neck Tumor Segmentation in PET/CT Challenge*. Springer, pp. 99–108. URL: https://link.springer.com/chapter/10.1007/978-3-030-98253-9_9, doi:https://doi.org/10.1007/978-3-030-98253-9_9.

Ma, H., Zhang, Q., Zhang, C., Wu, B., Fu, H., Zhou, J.T., Hu, Q., 2023. Calibrating multimodal learning, in: *International Conference on Machine Learning*, PMLR. pp. 23429–23450. URL: https://www.researchgate.net/publication/371290951_Calibrating_Multimodal_Learning.

Mukhoti, J., van Amersfoort, J., Torr, P.H., Gal, Y., 2021. Deep deterministic uncertainty for semantic segmentation. *arXiv preprint arXiv:2111.00079* URL: <https://doi.org/10.48550/arXiv.2111.00079>.

Nie, D., Wang, L., Gao, Y., Shen, D., 2016. Fully convolutional networks for multi-modality isointense infant brain image segmentation, in: *2016 IEEE 13th international symposium on biomedical imaging (ISBI)*, IEEE. pp. 1342–1345. URL: <https://ieeexplore.ieee.org/document/7493515>, doi:10.1109/ISBI.2016.7493515.

Oreiller, V., Andrearczyk, V., Jreige, M., Boughdad, S., Elhalawani, H., Castelli, J., Vallières, M., Zhu, S., Xie, J., Peng, Y., et al., 2022. Head and neck tumor segmentation in pet/ct: the hecktor challenge. *Medical image analysis* 77, 102336. URL: <https://www.sciencedirect.com/science/article/pii/S1361841521003819>, doi:<https://doi.org/10.1016/j.media.2021.102336>.

Paszke, A., Gross, S., Massa, F., Lerer, A., Bradbury, J., Chanan, G., Killeen, T., Lin, Z., Gimelshein, N., Antiga, L., et al., 2019. Pytorch: An imperative style, high-performance deep learning library. *Advances in neural information processing systems* 32. URL: https://proceedings.neurips.cc/paper_files/paper/2019/file/bdbca288fee7f92f2bfa9f7012727740-Paper.pdf.

Peng, Y., Sun, J., 2023. The multimodal mri brain tumor segmentation based on ad-net. *Biomedical Signal Processing and Control* 80, 104336. URL: <https://www.sciencedirect.com/science/article/pii/S174680942200790X>, doi:<https://doi.org/10.1016/j.bspc.2022.104336>.

Qayyum, A., Benzinou, A., Mazher, M., Abdel-Nasser, M., Puig, D., 2021. Automatic segmentation of head and neck (h&n) primary tumors in pet and ct images using 3d-inception-resnet model, in: *3D Head and Neck Tumor Segmentation in PET/CT Challenge*. Springer, pp. 58–67. URL: https://link.springer.com/chapter/10.1007/978-3-030-98253-9_4.

Rokach, L., 2010. Ensemble-based classifiers. *Artificial intelligence review* 33, 1–39. URL: <https://doi.org/10.1007/s10462-009-9124-7>, doi:10.1007/s10462-009-9124-7.

Saxe, A.M., McClelland, J.L., Ganguli, S., 2013. Exact solutions to the nonlinear dynamics of learning in deep linear neural networks. *arXiv preprint arXiv:1312.6120* URL: <https://doi.org/10.48550/arXiv.1312.6120>.

Shu, X., Wang, J., Zhang, A., Shi, J., Wu, X.J., 2024. Cscu u-net: A channel and space compound attention cnn for medical image segmentation. *Artificial Intelligence in Medicine* , 102800 URL: <https://www.sciencedirect.com/science/article/pii/S0933365724000423>, doi:<https://doi.org/10.1016/j.artmed.2024.102800>.

Van Amersfoort, J., Smith, L., Teh, Y.W., Gal, Y., 2020. Uncertainty estimation using a single deep deterministic neural network, in: *International conference on machine learning*, PMLR. pp. 9690–9700. URL: <https://proceedings.mlr.press/v119/van-amersfoort20a.html>.

Vaswani, A., Shazeer, N., Parmar, N., Uszkoreit, J., Jones, L., Gomez, A.N., Kaiser, Ł., Polosukhin, I., 2017. Attention is all you need. *Advances in neural information processing systems* 30. URL: https://proceedings.neurips.cc/paper_files/paper/2017/file/3f5ee243547dee91fbd053c1c4a845aa-Paper.pdf.

Wang, F., Cheng, C., Cao, W., Wu, Z., Wang, H., Wei, W., Yan, Z., Liu, Z., 2023. Mfcnet: A multi-modal fusion and calibration networks for 3d pancreas tumor segmentation on pet-ct images. *Computers in Biology and Medicine* 155, 106657. URL: <https://www.sciencedirect.com/science/article/pii/S0010482523001221>, doi:<https://doi.org/10.1016/j.combiomed.2023.106657>.

Wang, J., Peng, Y., Guo, Y., Li, D., Sun, J., 2021. Ccut-net: pixel-wise global context channel attention unet for head and neck tumor segmentation, in: *3D Head and Neck Tumor Segmentation in PET/CT Challenge*. Springer, pp. 38–49. URL: https://link.springer.com/chapter/10.1007/978-3-030-98253-9_2, doi:https://doi.org/10.1007/978-3-030-98253-9_2.

Wang, Y., Yu, B., Wang, L., Zu, C., Lalush, D.S., Lin, W., Wu, X., Zhou, J., Shen, D., Zhou, L., 2018. 3d conditional generative adversarial networks for high-quality pet image estimation at low dose. *Neuroimage* 174, 550–562. URL: <https://www.sciencedirect.com/science/article/pii/S1053811918302507>, doi:<https://doi.org/10.1016/j.neuroimage.2018.03.045>.

Wolterink, J.M., Leiner, T., Viergever, M.A., Išgum, I., 2017. Generative adversarial networks for noise reduction in low-dose ct. *IEEE transactions on medical imaging* 36, 2536–2545. URL: <https://pubmed.ncbi.nlm.nih.gov/28574346/>, doi:10.1109/TMI.2017.2708987.

Yu, Q., Shi, Y., Sun, J., Gao, Y., Zhu, J., Dai, Y., 2019. Crossbar-net: A novel convolutional neural network for kidney tumor segmentation in ct images. *IEEE transactions on image processing* 28, 4060–4074. URL: <https://ieeexplore.ieee.org/document/8668577>, doi:10.1109/TIP.2019.2905537.

Zhang, D., Huang, G., Zhang, Q., Han, J., Han, J., Yu, Y., 2021. Cross-modality deep feature learning for brain tumor segmentation. *Pattern Recognition* 110, 107562. URL: <https://www.sciencedirect.com/science/article/pii/S0031320320303654>, doi:<https://doi.org/10.1016/j.patcog.2020.107562>.

Zhang, W., Li, R., Deng, H., Wang, L., Lin, W., Ji, S., Shen, D., 2015. Deep convolutional neural networks for multi-modality isointense infant brain image segmentation. *NeuroImage* 108, 214–224. URL: <https://www.sciencedirect.com/science/article/pii/S1053811914010660>, doi:<https://doi.org/10.1016/j.neuroimage.2014.12.061>.

Zhang, X., Zhang, B., Deng, S., Meng, Q., Chen, X., Xiang, D., 2022. Cross modality fusion for modality-specific lung tumor segmentation in pet-ct images. *Physics in Medicine & Biology* 67, 225006. URL: <https://dx.doi.org/10.1088/1361-6560/ac994e>, doi:10.1088/1361-6560/ac994e.

Zhao, X., Li, L., Lu, W., Tan, S., 2018. Tumor co-segmentation in pet/ct using multi-modality fully convolutional neural network. *Physics in Medicine & Biology* 64, 015011. URL: <https://pubmed.ncbi.nlm.nih.gov/30523964>, doi:10.1088/1361-6560/aaf44b.

Zhong, Z., Kim, Y., Zhou, L., Plichta, K., Allen, B., Buatti, J., Wu, X., 2018. 3d fully convolutional networks for co-segmentation of tumors on pet-ct images, in: 2018 IEEE 15th International Symposium on Biomedical Imaging (ISBI 2018), IEEE. pp. 228–231. URL: <https://ieeexplore.ieee.org/abstract/document/8363561>, doi:10.1109/ISBI.2018.8363561.

Zhou, T., Ruan, S., Canu, S., 2019. A review: Deep learning for medical image segmentation using multi-modality fusion. *Array* 3, 100004. URL: <https://www.sciencedirect.com/science/article/pii/S2590005619300049>, doi:<https://doi.org/10.1016/j.array.2019.100004>.

Zou, K., Yuan, X., Shen, X., Chen, Y., Wang, M., Goh, R.S.M., Liu, Y., Fu, H., 2023. Evidencecap: towards trustworthy medical image segmentation via evidential identity cap. arXiv preprint arXiv:2301.00349 URL: <https://doi.org/10.48550/arXiv.2301.00349>.